

Review

Additive manufacturing of biodegradable magnesium implants and scaffolds: Review of the recent advances and research trends

Nurettin Sezer^{a,*}, Zafer Evis^b, Muammer Koç^{a,c}

^aDivision of Sustainable Development, College of Science and Engineering, Hamad Bin Khalifa University, Qatar Foundation, Education City, Doha, Qatar

^bEngineering Sciences, Middle East Technical University, PO Box 06800, Ankara, Turkey

^cUniversity of Karabiik, Turkey

Received 27 December 2019; received in revised form 17 May 2020; accepted 29 September 2020

Available online 6 November 2020

Abstract

Synthetic grafting needs improvements to eliminate secondary surgeries for the removal of implants after healing of the defected tissues. Tissue scaffolds are engineered to serve as temporary templates, which support the affected tissue and gradually degrade through the healing period. Beside mechanical function to withstand the anatomic loading conditions, scaffolds should also provide a decent biological function for the diffusion of nutrients and oxygen to the cells, and excretion of the wastes from the cells to promote the new tissue growth and vascularization. Moreover, the degradation byproducts of the scaffolds should be safe to the human body. Development of such multifunctional scaffolds requires selection of the right material, design, and manufacturing method. Mg has been recognized as the prominent biodegradable metal with regards to its mechanical properties matching to that of human bone, degradability in the body fluid, and its ability to stimulate new tissue growth. Scaffolds with intricate porous structures can be designed according to the patient-specific anatomic data using computer aided designs. Additive manufacturing (AM) is the right method to materialize these models rapidly with reasonably acceptable range of dimensional accuracy. Thus, the recent research trend is to develop ideal scaffolds using biodegradable Mg through AM methods. This review compiles and discusses the available literature on the AM of biodegradable Mg parts from the viewpoints of material compositions, process conditions, formation quality, dimensional accuracy, microstructure, biodegradation, and mechanical properties. The current achievements are summarized together, and future research directions are identified to promote clinical applications of biodegradable Mg through the advancement of AM.

© 2020 Chongqing University. Publishing services provided by Elsevier B.V. on behalf of KeAi Communications Co. Ltd.

This is an open access article under the CC BY-NC-ND license (<http://creativecommons.org/licenses/by-nc-nd/4.0/>)

Peer review under responsibility of Chongqing University

Keywords: Magnesium; Alloy; Implant; Tissue scaffold; Additive manufacturing; Biodegradation.

1. Introduction

With the self-healing ability, bone tissue undergoes remodeling, maturation, differentiation, and controlled resorption through a dynamic process [1]. This process contains osteoclasts and osteoblasts, which are responsible for maintaining tissue health. However, the ability of functional regeneration is considerably limited when the affected tissues are either completely destroyed by traumatic injuries or degenerated by

age-related or inflammatory diseases [2]. In such cases, the repair of bone tissue defects is very difficult, and usually external treatment such as autograft or allograft is required to restore previous form and functions [3]. In autograft, a bone taken from the same person's body is used, while in allograft, a bone taken from a deceased donor is used. Harvesting autograft tissue increases the morbidity to the patient associated with an additional surgical site, and allograft tissue carries the risk of infectious disease from the donor and depends on the availability of the donor and logistics. Thus, inadequacies of autograft and allograft tissue have led to greater research efforts towards developing biomimetic materials that are suit-

* Corresponding author.

E-mail address: nsezer@hbku.edu.qa (N. Sezer).

able for tissue repair without any intrinsic problems. In this context, tissue engineering is an emerging area of research, which typically involves the use of scaffolds to provide structural support to a newly forming tissue [4]. Scaffolds also serve as temporary templates to aid the diffusion of nutrients and oxygen to and excretion of the metabolic waste from the cells, as well as to form the extracellular matrix (ECM) in defected region. The quest for new developments in the design of these scaffolds can be realized by computer-aided designing using the patient-specific anatomic data. Suitable design of porosity, size and topology of each specific defect can be selected by computational modeling. Then, the designed scaffold can be materialized by AM technology.

Scaffolds can be produced using various types of materials such as polymers, ceramics, and metals [5–7]. Polymers possess good plasticity and biocompatibility but low strength, poor hydrophilicity, and aseptic inflammation risk restrict their applications in hard tissue repair [8,9]. Ceramics combine excellent bioactivity and biocompatibility but are usually limited by their high brittleness. Compared to ceramics and polymers, the high mechanical strength and fracture toughness of metals make them more suitable for load bearing applications such as joint replacement, bone plates and screws, tissue scaffolds, as well as dental root implants [10]. Currently, stainless steels, titanium, and cobalt–chromium-based alloys are the most commonly used metallic biomaterials [11,12]. However, the release of toxic and carcinogenic metal ions or particles during degradation process causes inflammation in human body that weakens the biocompatibility [13]. Also, the mismatch between the elastic moduli of metal and bone leads to stress shielding that deteriorates new bone stimulation and remodeling [14]. Further, after the completion of the healing process, the metallic biomaterials are removed by secondary surgical operation(s), which in turn increases the cost and morbidity to the patients [15–17]. Even in the case that metallic biomaterial is permanently fixed in the body and no additional surgery is required, bone regeneration may not be complete. Thus, biodegradability is considered one of the essential requirements of an ideal implant and scaffold [18].

1.1. Biodegradable metals

Biodegradable metals such as iron (Fe), zinc (Zn), and magnesium (Mg) have attracted special interest in biomedical research. Numerous studies have been performed to prepare biodegradable materials using the alloys of these metals. Pure iron has several advantages to be used as biodegradable metal such as good mechanical properties, biocompatibility, and biodegradability. It is also one of the essential elements for human life [19]. It has favorable mechanical properties. For example, the high elastic modulus of Fe leads to a high radial strength. However, the degradation rate of Fe is too slow to meet the requirements of tissue repair [18,20]. Higher degradation rate is desired for biodegradable Fe [20]. Thus, without modifying its corrosion rate, Fe is not suitable to be used in biomedical applications.

Zinc is another essential element of human life. It is present in several body tissues such as skin, muscle, liver, and bone. Infants and adults need around $2 \text{ mg}\cdot\text{day}^{-1}$ and $6.5\text{--}15 \text{ mg}\cdot\text{day}^{-1}$ of Zn, respectively for the basic biological functions such as DNA synthesis, nucleic acid metabolism, enzymic reactions, and apoptosis regulation etc. [21–23]. Besides, Zn corrodes at a moderate rate that can be controlled by adding several alloying elements or by applying forming processes. In the literature, it has been shown that the degradation rate of Zn is slower than Mg and faster than Fe, which makes Zn a good candidate to be used as degradable biomaterial. Therefore, Zn has recently attracted significant attention. Yet, the poor strength and ductility still restrict its use in load-bearing applications [5].

Mg is the prominent biodegradable material with exceptional performance [24–26]. It is also an essential element in human body [27], with daily intake of around 300–400 mg [25]. 25 mg Mg is stored in the body, half of which is stored in bone tissue [13], and the redundant magnesium cations can be effectively excreted in the urine [24]. It has been reported that the presence of Mg in the bone tissue promotes bone strength and stimulate bone growth [13,28]. With a density and Young's modulus of 1.7 g/cm^3 and 42 GPa, very similar to that of human bone; $1.8 - 2.1 \text{ g/cm}^3$ and 3 - 20 GPa, respectively, Mg is a promising material in biomedical applications [25].

The environment of a human body is very aggressive to metallic products. Despite many favorable intrinsic properties of Mg, its rapid degradation in body fluid or blood plasma causes uncontrollable hydrogen evolution and formation of gas pockets in scaffold-tissue interface, which delays or prevents the healing of the surgery region [29,30]. In addition, the local alkalization around the Mg-scaffold with increased OH^- ions due to rapid degradation can alter the physiological microenvironment and even lead to alkaline poisoning of the surrounding tissues when pH reaches above 7.8. Thus, controlling the degradation rate of Mg, so the generation rate of hydrogen gas and OH^- ions would be a good strategy to allow the human body to progressively adjust or deal with the biodegradation byproducts [20,24].

1.2. Biodegradable Mg alloys

Mg alloys are known as the lightest structural alloys [31]. These alloys are composed of Mg, the lightest structural metal, and some other elements, such as silicon, aluminum, rare-earth elements, zinc, manganese, zirconium, and copper, so as to enhance the physical properties [32]. The exceptional properties of Mg alloys such as high strength-to-weight ratio, high stiffness-to-weight ratio, lightweight, machinability, castability, and great damping allow them to be used in variety of industries including automotive, electronics, defense, and aerospace.

Cast Mg alloys are widely used in the interior and powertrain components of the automotive industry and constitute the major magnesium alloys used today. Whereas, wrought

Mg alloys are less used because of the poor formability and high cost [33].

Rare earth elements, such as Nd, Y, Ce, and Gd, are used as major alloying elements in cast magnesium alloys. These elements possess relatively high solubility in Mg and are effective in precipitation hardening and creep resistance [33]. The prevailing cast magnesium alloys can be listed as: AZ63, AZ81, AZ91, AM50, ZK51, ZK61, ZE41, ZC63, HK31, HZ32, QE22, QH21, WE54, WE43, and Elektron 21, whereas typical wrought magnesium alloys are AZ31, AZ61, AZ80, Elektron 675, ZK60, M1A, HK31, HM21, ZE41, and ZC71. The prefix letters define two principal alloying metals in magnesium alloys that were developed according to ASTM B275 where A: Aluminum, B: Bismuth, C: Copper, D: Cadmium, E: Rare earths, F: Iron, H: Thorium, K: Zirconium, L: Lithium, M: Manganese, N: Nickel, O: Silver, R: Chromium, S: Silicon, T: Tin, W: Yttrium, and Z: Zinc [34].

In biomedical applications, alloying is the commonly practiced method for controlling the degradation rate of Mg [32,35]. Careful selection of the alloying elements can significantly enhance the degradation resistance and mechanical properties of Mg [13,35]. Mg alloys can be classified in two main groups. First group contains 2–10 wt% Al with trace amount of Mn and Zn, which exhibits enhanced mechanical properties and moderate degradation resistance. Second group contains mixture of rare earth elements together with a different metal such as Y, Zn, or Ag, and a lesser amount of Zr, which leads enhanced mechanical performance, finer grain structure, and improved degradation resistance [13,36,37].

Most studies indicated that alloying is a promising method for controlling the degradation rate of Mg without compromising its favorable intrinsic properties. For instance, AZ31B, produced by alloying Mg with Al and Zn, improved the in vivo degradation resistance inside the femora of rabbits [38]. Hampp et al. [39] studied LANd442 alloy with a composition of 90 wt% Mg, 4 wt% Li, 4 wt% Al, and 2 wt% Nd. An improved corrosion resistance with formation of new bony tissue was observed in a rabbit model. However, small amount of subcutaneous gas was detected in the implant region. Li et al. [40] showed that addition of <2wt% Sr considerably improves corrosion resistance for Mg–Zr–Sr and Mg–Sr alloys. Incorporation of Sr is also found to improve the corrosion resistance of Mg–5Al alloys [41]. In vitro studies by Bornapour et al. [42] showed the formation of a Sr-hydroxyapatite (HAp) layer on the surface of the binary Mg–Sr alloy after immersion in simulated body fluid (SBF). This bioactive surface layer improved the corrosion resistance. After investigating the corrosion behavior and mechanical properties of MgNd₂ alloy, Seitz et al. [43] suggested Nd₂ as a suitable alloying element of Mg for bioresorbable applications but not for load bearing applications.

Bone growth can be promoted by incorporation of Ca in Mg alloy, and the mechanical and corrosive properties of Mg–Ca alloys can be manipulated by changing the Ca content. Li et al. [44] prepared binary Mg–Ca alloy with Ca content varying from 1 to 20wt%. Mg–1Ca alloy induced no toxicity to cells. Apatite layer was formed on the surface of Mg–1Ca al-

loy, which improved corrosion resistance. Similarly, Rad et al. [45] observed enhanced corrosion after adding 0.5% Ca in Mg.

Biodegradable Mg alloys with various compositions investigated thus far revealed favorable results. Careful selection of the type and content of the alloying element(s) can significantly improve the biodegradation resistance of Mg without compromising its biocompatibility and mechanical function.

Mg and its alloys have attracted special interest for temporary implant applications such as bone plates and screws in orthopedics and as stents in cardiovascular implantology. Biodegradable fixation hardware made of Mg alloy can be a good alternative to today's stiff bone fixation hardware [32]. Mg alloy can provide adequate support to the bone through the healing period and degrade gradually.

For cardiovascular applications, CE-approved biodegradable Mg-based vascular closure device, named as “Velox CD”, has been developed through transluminal technologies [46]. Ureteral stents and coronary scaffolds are other examples to the application of Mg alloys in biomedical [47,48]. Wang et al. [49] used Mg alloy (Mg–Zn–Y–Nd) stent for the treatment of esophageal cancer. Mg alloy inhibited the growth of esophageal cancer cells and possessed good biodegradability and milder hardness than 317L stainless steel.

Zhao et al. [50] investigated the potential of applying pure Mg screws for the fixation of vascularized bone graft in osteonecrosis of the femoral head (ONFH) patients. According to the results, Mg screw is found to be biocompatible and effective in stabilizing bone flap. Its degradation rate is tolerable by the tissue healing rate, and the released Mg ions stimulate new bone formation.

Various types of materials are available for airway stenting, including silicone, metallic, and hybrid tubes. Though, none of these stents provides satisfactory long-term effectiveness. Non-degradable silicone tubes interfere with the mucociliary clearance and metallic stents cause undesirable tissue ingrowth and formation of severe granulation. These complications often necessitate secondary surgical procedures for removal of the stents. Due to the obvious deficiencies of currently available stents, there is a significant clinical need for a biodegradable airway stents that would maintain airway patency and totally degrade overtime after fulfilling the desired objectives. Wu et al. [51] studied the feasibility of biodegradable magnesium alloys for tracheal stent application. The study identified Mg alloys (magnesium-aluminum-zinc-calcium-manganese (AZXM)) to show excellent cytocompatibility and found AZXM to be a promising candidate in tracheal stent applications.

Yuan et al. [51] developed a biodegradable magnesium alloy (Mg–Nd–Zn–Zr) nerve conduit for peripheral nerve defect repair and implanted it into the defect area of sciatic nerve of adult SD rat. 2 months after implantation, good nerve regeneration, no scar tissue or inflammatory response around, and no bubble formation were observed.

The above-summarized literatures are few examples to the application of Mg alloys in biomedical field. It is believed that Mg and its alloys are a new generation of biomaterials

that will play a significant role in revolutionizing biomedical applications through suitable design and manufacturing [52].

1.3. Tissue scaffolds

The capacity of the functional tissue regeneration is very limited in the case of severe destruction or degeneration as mentioned before. Scaffolds are engineered to restore or replace the damaged or diseased tissue with a healthy and well-functioning tissue. Ideal tissue scaffolds should have the following five essential characteristics:

1. To have mechanical properties matching to that of the surrounding tissues to meet anatomic loading conditions in order to eliminate stress shielding and loosening of the scaffold [35].
2. To have suitable surface features such as wettability and roughness to enable attachment, proliferation, and differentiation of new cells [53].
3. To have highly porous, well-defined interconnected networks to provide sufficient permeability for the ingrowth of cells in three-dimensional architecture, diffusion of oxygen and nutrients to and excretion of metabolic wastes from the cells [20,54,55].
4. To be biodegradable or bioresorbable with a controllable degradation and resorption rate to match the cell/tissue growth rate [56,57].
5. To be biocompatible to prevent immunological or foreign body reactions [35,56].

Considering these essentials, development of an ideal tissue scaffold necessitates careful material selection, model design, and manufacturing. A suitable material can be selected based on its biocompatibility, biodegradability, and mechanical properties according to the clinical requirements. Computational modeling can be used to design optimum porous scaffold topology consistent with the patient-specific anatomic data. The applied manufacturing method should be capable of building models generated by computer design and using the selected material with high dimensional accuracy.

1.4. Additive manufacturing

AM, solid free-form fabrication, and 3D printing are synonymous [58], and have been considered an ideal solution for manufacturing complex 3D porous architectures with a precise control over pore topology [58–60]. AM is capable of fabricating versatile scaffolds with intricate geometrical shapes, which can promote uniform cell distribution and mimic the ECM. It employs a layer-by-layer fabrication process from computer aided design (CAD) models [61]. There are several types of AM processes depending on the feedstock materials (powder or wire) and heat sources (laser, electron beam or arc) used. ASTM Standard F2792 classifies the AM processes in two groups as Powder Bed Fusion (PBF) and Directed Energy Deposition (DED) [62]. PBF is considered as one of the near net shape fabrication methods [63], and

the mostly preferred AM method for the manufacturing of metallic scaffolds. It employs thermal energy through different technologies such as selective laser melting (SLM) and electron beam melting (EBM) to selectively melt and fuse metal powders together in layers in a powder bed to form a solid pattern [14,60,64]. A layer of powder is spread over the building platform and selectively melted in a desired pattern. Then, the building platform is lowered to a preset distance by a piston to spread and selectively melt the next layer of powder on the preceding layer [65]. These steps are repeated with successive layers of powder until the desired material is completely built [28]. Typical thickness of each powder layer ranges from 20 to 100 μm . The powder that remains unaffected by the laser serves as a natural support for the model and remains in place until the model is complete. A shielding gas such as nitrogen or argon continuously flows through the build chamber to ensure high purity by minimizing oxygen and hydrogen in the environment, as well as to dissipate the heat and provide rapid cooling in the build chamber [60,64].

This review aims to compile and analyze the available literature on AM of biodegradable Mg alloys and composites for biomedical implants and scaffolds. Recent research on AM of biomedical Mg implants and scaffolds, and their formation quality and microstructural, mechanical and biological properties are reviewed and discussed. Opportunities and challenges of AM of Mg are presented. Briefly, this paper is a comprehensive review that compiles, analyzes, and critically discusses the recent literature on the important aspects of AM of biodegradable implants and scaffolds made of Mg, its alloys and composites.

2. Additive manufacturing of Mg scaffolds

Despite many potential advantages of biodegradable metal scaffolds, their manufacturing in three-dimensional porous architecture with customized micro- and macro-scale geometry is the major challenge. The conventional manufacturing methods, such as powder metallurgy, sintering, foaming, casting, chemical vapor deposition, and electrodeposition fall short of controlling the pore dimensions and the customized geometry of the scaffolds that must match the anatomy of the patient [20]. Thus, conventional manufacturing methods can process only randomly organized porous structures, which do not allow precise control over pore architecture, and are not suitable for optimizing scaffold properties such as porosity, permeability, mechanical strength, and stiffness [20,59]. The random porous structures cannot possess homogenous biological and mechanical properties especially at the micro scale [59], which may cause undesirable material behavior such as strut bending and twisting [66]. However, AM allows fabrication of interconnected porous metal scaffolds with the customized external shape and internal architecture [20,55]. These scaffolds possess much superior mechanical and biological properties than those processed through conventional methods [36,55].

A first ever study on AM of Mg was reported by Ng et al. [67] in 2010. They reported successful melting of single tracks of Mg layer. Later, many articles have been published

on AM of Mg, its alloys and composites using mainly SLM process, as well as other processes such as Selective Laser Sintering (SLS), binder-jetting, and indirect processes. Today, owing to its ability to build customized shapes with intricate structures in high dimensional accuracy, AM is attracting more interest in fabricating Mg scaffolds. This section summarizes the present researches on AM of biodegradable Mg-based implants, and scaffolds based on the applied manufacturing processes.

2.1. Selective laser melting

SLM process involves rapid heating and cooling cycles that typically reaches above 10^5 K/s [68,69]. Thus, the grain growth is inhibited through a rapid solidification at such high cooling rates [70]. It also reduces the composition segregation, allowing a homogeneous microstructural architecture through the scaffold. Dense and homogeneous microstructure, in terms of phase morphology and grain size favors enhanced densification, mechanical properties, and degradation resistance [71]. Liu et al. [72] studied manufacturing of porous Mg-Ca alloys by SLM. Due to the grain refinement and solid solution strengthening, microhardness of SLM-produced sample was superior to that of as-cast pure magnesium.

WE43 is a biodegradable Mg alloy with addition of Y and rare earth elements, and it has been clinically verified [73]. Zumdieck et al. [74] investigated the properties of SLM produced WE43 in comparison to the traditional manufacturing methods. The SLM-produced samples showed an extremely fine grains and homogeneous microstructure with grain sizes of around $1\ \mu\text{m}$ and very fine secondary phases whereas the as-cast sample possessed much larger grain size $44.3\ \mu\text{m}$ and different phases. Tensile tests of the additively manufactured samples possessed an improved ultimate tensile strength of 308 MPa and 12% elongation to failure. Another investigation of SLM-produced WE43 alloy was conducted by Bär et al. [36], which showed an improved biodegradation resistance in comparison to the as cast counterparts. The studies suggested that SLM is a suitable process to fabricate Mg parts with enhanced microstructure, mechanical properties, and biodegradation performance due to the rapid heating and cooling inherent to the SLM process.

Zn-containing magnesium alloy with satisfactory mechanical properties can be developed into a biodegradable material [24]. In this regard, Chen et al. [71] fabricated binary Mg-Zn alloys by SLM, and studied the mechanical and corrosive properties. The SLM processed alloy exhibited homogenous grains, with an average size of $15\ \mu\text{m}$. Grain growth was effectively inhibited by the precipitation of the MgZn phase and rapid solidification. Finer grains reduced the degradation rate and enhanced the microhardness. Mg-Zn binary alloys with varying Zn content was studied by Wei et al. [75] using SLM process. Near full dense parts were obtained at Zn content 1 wt%. Mg-1Zn sample possessed comparable mechanical properties to that of the as-cast counterpart.

The corrosion resistance of Mg-Zn can be enhanced by alloying with Al. AZ31, AZ61, and AZ91 are the common

Mg-Al-Zn alloys with moderate corrosion rates. He et al. [76] studied fabrication of Mg-Al-Zn (AZ61) alloy using SLM. Uniformed equiaxed grains were achieved at laser input energy 80 W, which revealed minimum mass loss $12.26\ \text{mg}\cdot\text{cm}^{-2}$ after immersion in SBF for 144 h, and maximum microhardness 93.00 HV. Further, apatite formation was observed on the surface of AZ61 alloy. In the study of Liu et al. [77], AZ61 magnesium alloys (Mg-6Al-1Zn) with the addition of Y (0–4wt%) were fabricated using SLM. The degradation resistance of the AZ61 alloy was improved by the addition of Y element. The optimal degradation and hardness were achieved at 2wt% Y. Zhang et al. [78] manufactured Mg-9wt%Al alloy with >99.9% relative density using SLM. A hardness value of 75 HV was reported as compared to that of as-cast AZ91 alloy 60 HV. Wei et al. [63] built AZ91D alloys without obvious macro-defects using SLM. Mechanical properties of the SLM-processed AZ91D were superior to that of the die-cast AZ91D due to the grain refinement and solid solution strengthening.

Another way of improving the corrosion resistance of Mg-Zn alloys is incorporating HAp ($\text{Ca}_{10}(\text{PO}_4)_6(\text{OH})_2$) [79,80]. In this respect, Shuai et al. [81] prepared Mg-3Zn/xHA composites using SLM process. Relative density of the as-built samples ranged from 95.5% - 97.9%. Rapid solidification prevented agglomeration of HA particles and promoted homogeneous dispersion. Increasing HA content lead to the formation of finer grains. Finer grains together with the formation of apatite coating layer lead to improved biodegradation resistance. Further, hardness of Mg-3Zn alloy was improved through fine grain strengthening and second phase strengthening.

Zr is another alloying element for Mg-Zn alloys to reduce the grain size and degradation rate [82–84]. Zhang et al. [85] prepared porous Mg-Zn-Zr (ZK61) alloys at varying Zn content using SLM. A relatively high surface quality was acquired at laser energy density ranging from $1019\ \text{J}/\text{mm}^3$ to $1146\ \text{J}/\text{mm}^3$. Shuai et al. [16] used SLM process to prepare ZK60-Cu alloy, which possess excellent antibacterial properties and favorable corrosion in body fluid. ZK60–0.4Cu alloy had an improved compressive strength due to grain refinement strengthening, precipitate strengthening, and dispersion strengthening. The cell culture experiments revealed that ZK60-Cu alloy has good cytocompatibility.

Long et al. [86] prepared Mg-3Zn-xDy ($x=0 - 5\text{wt}\%$) alloys using SLM process. Degradation and hydrogen evolution rate of the Mg-3Zn-1Dy alloys was remarkably reduced due to the combined effect of smaller grain size, homogeneous microstructure, and the presence of the second phase. Shuai et al. [87] prepared Mg-Sn-Zn alloys at varying Zn content using SLM. The SLM processed Mg-Sn alloys showed finer grains than as-cast and as-rolled Mg-Sn alloys. With increasing Zn content up to 4wt%, degradation resistance of the alloys improved due to grain refinement and the formation of $\text{Zn}(\text{OH})_2$ protective layer. Zn also increased the hardness of the alloys owing to the grain refinement strengthening and solid solution strengthening.

Li et al. [88] fabricated topologically ordered porous magnesium (WE43) scaffolds based on the diamond unit cell by

SLM process. Scaffolds were designed with strut size $400\ \mu\text{m}$, pore size $600\ \mu\text{m}$ to yield 67% porosity, while the as-built scaffolds possessed an average strut size $420\ \mu\text{m}$ and porosity 64%. Mechanical properties of the porous WE43 ($E=0.7\text{--}0.8\ \text{GPa}$) scaffolds were found to fall into the range of the values reported for trabecular bone ($E=0.5\text{--}20\ \text{GPa}$) even after 4 weeks of biodegradation. The actual topology of the porous structures closely matched the designed topology including a fully interconnected porous structure, high porosity, and precisely controlled geometry of the unit cells. Additively manufactured porous Mg specimens showed a satisfactory biodegradation behavior with about 20% volume loss after 4 weeks. Limited cytotoxicity of less than 25% was reported. In a follow up study, fatigue behavior of the same scaffold was investigated in r-SBF and in air [89]. Biodegradation affected the fatigue resistance of the additively manufactured WE43 magnesium alloy scaffolds and reduced the fatigue strength from $0.3\sigma_y$ to $0.2\sigma_y$. Cyclic loading accelerated the biodegradation process in r-SBF. The study pointed that the fatigue properties of the biodegradable scaffolds can be improved by optimizing the topological design and laser processing parameters that greatly affect the microstructure of the porous scaffolds. Qin et al. [73] mechanically mixed WE43 and pure Zn powders to fabricate porous Zn-xWE43 ($x=0\%$, 2%, 5% and 8%) scaffolds by SLM. High densification of above 99.9% was reported for the as-manufactured Zn-WE43 scaffold. Rapid cooling rate and the addition of WE43 remarkably refined the grain size. Molten Zn easily took a capillary action among powders and sintered the surrounding powders together. Therefore, a lot of powders attached to the molten pool, which increased the strut diameter compared with the design value. Thus, there was a big difference between the geometrical porosity of as-designed 67% and as-built 45% scaffolds. The fracture behavior of the porous scaffold was found to be directly related to the structural design.

The reviewed literature shows that SLM is a promising method to fabricate Mg-based parts using Mg powders of a wide variety of chemical compositions. A number of different Mg alloys have been successfully built by SLM. Researches also show that the mechanical and corrosive properties of the as-built SLM parts are superior to the counterparts fabricated by traditional methods that is discussed in detail in Section 3.3 and Section 3.4. In addition to building bulk Mg cubes, SLM also allows for building porous Mg scaffold models with a well-defined interconnected network in high dimensional accuracy.

2.2. Selective laser sintering

Selective laser sintering (SLS) is another type of powder-based AM that uses laser to sinter powder particles, thereby binding the material together to form a solid structure [90]. The major difference between the SLS and SLM processes is that laser scanning in SLM involves complete melting of powder particles, whereas they are partially melted and re-solidified in SLS. Tsai et al. [91] incorporated magnesium-calcium silicate (Mg-CS) powder into poly- ϵ -caprolactone

(PCL) to manufacture 3D porous bioactive Mg-CS/PCL scaffolds by SLS process. The wettability and degradation rates of PCL were improved by the incorporation of Mg-CS powder. Mg-CS content significantly stimulated the new bone growth in SBF. Biocompatibility of the scaffold samples was confirmed by in vitro studies with human mesenchymal stem cells (hMSCs).

Poly-L-lactic acid (PLLA) is a promising bone repair material owing to its good biocompatibility and natural degradability. However, the poor mechanical properties due to its poor crystallinity and local inflammatory response due to its acid degradation byproducts limit its application in tissue scaffold. To eliminate these limitations, Shuai et al. [92] incorporated magnesium oxide nanoparticles (nMgO) into PLLA to manufacture PLLA/3nMgO scaffold using SLS method. nMgO exhibited a good affinity to PLLA and served as a nucleating agent during crystallization process to enhance the crystallinity of PLLA. The tensile strength, Elastic modulus, and Vickers hardness of PLLA/3nMgO was enhanced by 38%, 24% and 11%, respectively, as compared with PLLA. Further, nMgO neutralized the acid degradation byproducts of PLLA that can prevent local tissue inflammation after implantation. Improved biocompatibility of PLLA/nMgO scaffolds was observed in vitro cell culture. Another study incorporated nMgO into poly(3-hydroxybutyrate-co-3-hydroxyvalerate) (PHBV) to manufacture 3D porous PHBV/nMgO scaffolds by SLS [93]. The SLS processed scaffold exhibited a well-ordered interconnected microporous structure. The presence of nMgO imparted strong antibacterial activity to the scaffold and enhanced the compressive strength of the PHBV scaffolds by 96% at 5 wt% nMgO loading. nMgO similarly neutralized the acid degradation byproducts of PHBV and promoted biodegradation of the scaffolds. Further, nMgO stimulated cellular adhesion, proliferation, and differentiation. Sun et al. [94] incorporated wollastonite (CaSiO_3) into Mg_2SiO_4 to fabricate MgO-CaO-SiO₂ scaffolds via SLS. The as-built scaffold exhibited a well interconnected porous network, favorable cell adhesion and proliferation. It was noted that addition of CaSiO_3 enhanced the densification, degradability, and bioactivity of the scaffold.

There are limited studies on the manufacturing of biodegradable Mg parts using SLS process. Generally, SLS processed scaffolds exhibit poor formation quality due to partial melting of particles that cannot fully infiltrate into the voids, thereby leave formation pores inside bulk metal and struts. Thus, SLS processed implants and scaffolds possess relatively low densification and poor mechanical properties, which restricts their use in load bearing orthopedic applications [1].

2.3. Binder jetting

Binder jetting is one of the AM methods, which employs a two-step process. The first step includes binding of powder through adhesion and chemical reaction mechanisms through a specified region in each progressive layer [95]. For adhe-

sion, a polymeric binder material either in a liquid or solid form is used to glue particles [96–98], while in the case of chemical reaction, particles react with a selectively deposited solution to bond together in specified regions [99,100]. As with other powder-based manufacturing methods, the object being printed is self-supported within the powder bed and is removed from the unbound powder once the process is complete. In the second step of binder jetting, the binder is removed through a debinding process, followed by post-treatment processes such as sintering [101–103], infiltration with a second material [104], and HIP [105] for densification.

Magnesium phosphate $Mg_3(PO_4)_2$ is a bioceramic with exceptional biocompatibility, bioactivity, and biodegradability [106]. Farag and Yun [107] developed a gelatin/ $Mg_3(PO_4)_2$ composite scaffold via binder jetting. The addition of up to 6 wt% gelatin into $Mg_3(PO_4)_2$ induced the formation of dense struts, thus significantly improved the mechanical properties of the scaffolds. In addition, the composite scaffolds exhibited good wettability and cell affinity. Vorndran et al. [108] applied binder jetting on $Mg_3(PO_4)_2$ powder with a binder liquid containing 2M K_2HPO_4 , 0.5M $(NH_4)_2HPO_4$ or 20% H_3PO_4 to form a matrix of either struvite-(K) ($MgKPO_4 \cdot 6H_2O$), struvite ($MgNH_4PO_4 \cdot 6H_2O$) or newberyite ($MgHPO_4 \cdot 3H_2O$) by a hydraulic setting reaction. Post-hardening process increased the compressive strength of struvite and newberyite scaffolds to 10MPa and 35MPa, respectively compared to the initial strengths of the as-built samples in a range of 1.3–2.8MPa. Despite the good mechanical properties achieved with the newly developed scaffolds, the study lacks cell viability and biocompatibility tests to assess their application potential in tissue engineering. Meininger et al. [109] applied binder jetting process to fabricate $Mg_3(PO_4)_2$ and Sr-substituted $Mg_3(PO_4)_2$ -based biodegradable scaffolds with pure water as the binder. Sintering and hardening processes were applied to the additively manufactured samples. Highly interconnected porous topology with an average pore size of $20\mu m$ was achieved. No compromise of mechanical strength was observed after substituting Sr in magnesium phosphate cement. In vitro tests showed a reduced release of Mg^{2+} and improved corrosion resistance with the incorporation of Sr.

Salahi et al. [110] developed a capillarity-driven bridging method which aided in rapid assembling of Mg particles into 3D structures with least metallurgical complexity. This method converted the MgO film on the outermost layer of Mg powder into inter-particle bridges. The concept was based on relating the physical properties of Mg powder feedstock to the amount of liquid required for the formation of capillary-driven bridges. Capillary-mediated assembly of powder particles eliminated the use of polymeric binders and maintained the overall composition of powder materials constant. Mg-5.9Zn-0.13Zr powder and a single-phase solvent were used to manufacture Mg alloy scaffold through binder jetting by Salahi et al. [111]. The interactions between the solvent and superficial particle layer in the powder bed enabled capillary-mediated binderless assembling of particles in each layer. Af-

ter completion of printing, the as-built scaffold was sintered to decompose interparticle networks.

Binder-jetting employs a two-stage process for fabricating 3D parts. The use of sacrificial binders for binding the powders together and the requirements of an additional process to remove the binder are the drawbacks of this method. Parts produced with the binder-jetting technology are basically particles glued together resulting in fragile structures with limited mechanical performance. Thus, post-processing is needed for densification. In binder jetting, due to the method of binding, the material characteristics are generally not suitable for structural parts and despite the relative speed of printing, additional post processing can add significant time to the overall process.

2.4. Indirect additive manufacturing

Infiltration can be employed as an indirect method for 3D manufacturing of Mg scaffolds. Firstly, a 3D CAD model with desired architecture is developed. Then, a positive polymeric template of the CAD model is manufactured by AM. This polymeric template is infiltrated with NaCl paste. The template is then removed by heating, and NaCl is sintered to form a negative NaCl template. Liquid Mg is casted into this template with an applied pressure, followed by dissolving NaCl to finally obtain the Mg scaffold [112].

An open-cell porous Mg with a dimensional accuracy 88–95% and fine macroscopic features 0.8mm was successfully manufactured using infiltration method by Staiger et al. [113]. Nguyen et al. [59] also manufactured topologically ordered porous Mg, which showed a smaller difference of 2.5% - 8.3% in dimensions from CAD models to Mg scaffolds. Compared to the initial design, there was a maximum of 6.1% reduction in porosity in Mg scaffolds. Owing to the rough surface topography (10.2mm) of the manufactured scaffolds, the surface area increased by 70%.

Oosterbeek et al. [114] studied a topologically ordered magnesium-biopolymer composite. First, a porous Mg cylinder with 2mm square pores and 1.5mm-thick struts was fabricated to yield a theoretical porosity of 59.6% through infiltration method. Then, porous Mg structure was molded with polylactic acid (PLA) through injection to produce Mg-PLA composite. Mg/PLA composite showed reduced lower yield strength and corrosion resistance than Mg. It was suggested that PLA is not a suitable biopolymer to be used in this composite system. Lin et al. [115] manufactured CoCr scaffolds (porosity: 80 vol%, pore size: $700\mu m$, inner diameter: 24mm) using SLM method, and infiltrated the scaffolds with Mg-3Al-1Zn (AZ31) alloy at $750^\circ C$ in inert atmosphere, using pressure-less infiltration method. The infiltrated composite was almost completely dense and demonstrated superb mechanical properties. The degradation of magnesium filler lead to a progressive reduction in the mechanical strength of the composite. However, it was observed that the degradation rate of the composite was much greater than pure AZ31 alloys due to galvanic corrosion, composite interface, and surface area.

The degradation of AZ31 resulted in reduced stiffness and strength.

Despite 3D printing of the polymer mold then infiltration of salt paste inside the printed mold, Kleger et al. directly printed NaCl templates with a structured porosity [116]. Stable NaCl paste with suitable flow behavior was prepared with the aid of surfactants. Printed NaCl paste was sintered, then infiltrated with Mg melt. Later, the NaCl template was removed by leaching in aqueous NaOH solution. The strut size of the NaCl template and the respective pore size of the Mg scaffold were found to correlate closely with a maximum mismatch of 0.03 mm. This corresponds to a difference less than 7%. Dimensional accuracy of the overall process was therefore found to be limited by the 3D-printing precision of the NaCl template rather than by the infiltration capabilities of the Mg melt.

Infiltration method holds the advantage of eliminating the use of Mg powder, which exhibits a volatile and explosive nature that are discussed in Section 4. However, in infiltration method, the geometric features such as pores and struts are limited to macro-scale, which may not be suitable in biomedical applications since open porous structures with micron-scale pores and struts are required for good biological performance. Also, topological discrepancies between the as-designed and as-built scaffolds, reported in the indirect manufacturing of Mg scaffolds, result in different pore size and strut thickness, which substantially impact cell ingrowth and mechanical integrity [117–121]. The advantages and challenges for AM of Mg are summarized in Table 1.

3. Properties of additively manufactured Mg

A number of materials and processes for AM of biodegradable Mg has been investigated. The mechanical and biological performance of the final products are greatly influenced by microstructure, design geometry, and dimensional accuracy of the manufacturing method, as well as the formation quality. In this section, the performance of additively manufactured Mg-based biodegradable materials is extensively reviewed and discussed.

3.1. Formation quality

Densification is a term used for the assessment of formation quality and optimization of the process parameters. Densification is the prevention of defects, which are random and separated pores, so-called processing pores, resulted by improper processing conditions. The undesired processing pores inside the struts can deteriorate the biological and mechanical performance of the Mg-based scaffolds [28,73]. Thus, a better formation quality can be attained by a more stable process and increased densification [122,123]. In the literature, relative densities greater than 99.5% have been achieved in SLM processed bulk metals [60,124]. The recent literature on the formation quality of additively manufactured Mg is given in Table 2. AM has been able to build Mg alloys with a relative density as high as above 99.9%.

3.2. Microstructure

The microstructure significantly effects the physical properties such as strength, toughness, ductility, hardness, as well as the wear and corrosion resistance of a material. The microstructure of the additively manufactured Mg parts is determined by the chemical composition of the powder material and processing conditions. High cooling rates involved in SLM results in much finer grains than those achievable with conventional methods. Ng et al. [125] reported enhanced microstructure by SLM of single track Mg due to high cooling rate and rapid solidification. SLM-produced WE43 exhibited much finer grain size 0.4 - 2.9 μm, as compared to as-cast counterparts 44 μm [74]. Similarly, Wei et al. [63] achieved an average grain size 1.2 μm with SLM produced AZ91D, whereas die-cast counterparts possessed much coarser grain size 57 μm.

The recent literature on the microstructural studies of additively manufactured Mg is summarized in Table 3. High cooling rates favored improvement of microstructure and physical properties in manufacturing of Mg alloys [126,127]. The grain size of the additively manufactured Mg-based parts ranged from sub-micron to 30 μm, much finer than the counterparts (40 – 300 μm) produced through the traditional methods. Besides, typical microstructural characteristics of additively manufactured Mg parts are refined grains, enhanced solid solution, and homogenized microstructure owing to the high cooling rate and rapid solidification during SLM process. These factors have dominant effect on the mechanical and corrosive properties of Mg. Thus, improved microstructure favors superior biological and mechanical functions that are discussed in the following sections.

3.3. Biodegradation

Biodegradation performance of the additively manufactured Mg depends on the selected material, design, and manufacturing process. In addition, processing conditions have dominant effect on the biodegradation characteristics of the as-built parts. Niu et al. [128] investigated the corrosion behavior of bulk pure Mg fabricated by SLM. The study emphasized the importance of selecting suitable parameters for SLM processing of Mg to minimize processing pores and corrosion rate. The corrosion rate (r) is calculated by the following equation:

$$r = (M_1 - M_2)/t_i \quad (1)$$

where M_1 and M_2 are the material mass before and after corrosion, respectively, and t_i is the immersion time.

Previous studies show that corrosion rate of Mg alloys can be reduced through grain refinement [129]. As mentioned earlier, SLM process involves rapid cooling, which lead to the formation of fine grains and homogenized microstructure [77] that favors enhanced corrosion resistance. Li et al. [88] successfully fabricated WE43 scaffolds using SLM method. The as-built scaffolds exhibited enhanced biodegradation resistance 0.17 ml/cm²-day compared to the

Table 1
Benefits and drawbacks of technologies for AM of biodegradable Mg.

Technology	Benefits	Drawbacks
Selective laser melting	<ul style="list-style-type: none"> • It does not need the use of support structures. • Powder can be recycled. • Rapid heating and cooling cycles lead to rapid solidification, which reduce composition segregation and allows for the formation of a homogeneous microstructural architecture through the scaffold. • Dense and homogeneous microstructure, in terms of phase morphology and grain size favors enhanced densification, mechanical properties, and degradation resistance. • SLM allows for well-defined interconnected network in high dimensional accuracy. 	<ul style="list-style-type: none"> • Vigorous evaporation can disturb very lightweight Mg powder bed. • High chemical reactivity of Mg can cause serious dust explosions. • The process consumes high energy. • Slow process due to the need of powder preheating, vacuum generation, and cooling off periods.
Selective laser sintering	<ul style="list-style-type: none"> • It does not need the use of support structures. • Powder can be recycled. 	<ul style="list-style-type: none"> • Vigorous evaporation can disturb very lightweight Mg powder bed. • High chemical reactivity of Mg can cause serious dust explosions. • The process consumes high energy. • Slow process due to the need of powder preheating, vacuum generation, and cooling off periods. • Poor formation quality due to partial melting of particles that cannot fully infiltrate into the voids. It leaves formation pores inside bulk metal and struts. • Low densification and poor mechanical properties, which restricts their use in load bearing orthopedic applications.
Binder jetting	<ul style="list-style-type: none"> • The process is generally faster than others. 	<ul style="list-style-type: none"> • The use of sacrificial binders for binding the powders together and the requirements of an additional process to remove the binder are the drawbacks of this method. • Parts produced with the binder-jetting technology are particles glued together resulting in fragile structures with limited mechanical performance. Post-processing is required for densification. • Due to the method of binding, the material characteristics are generally not suitable for structural parts. • The geometric features such as pores and struts are limited to macro-scale, which may not be suitable in most biomedical applications since open porous structures with micron-scale pores and struts are required for good biological performance. • Topological discrepancies between the as-designed and as-built scaffolds, reported in the indirect manufacturing of Mg scaffolds, result in different pore size and strut thickness, which substantially impact cell ingrowth and mechanical integrity.
Indirect additive manufacturing	<ul style="list-style-type: none"> • Infiltration method holds the advantage of eliminating the use of Mg powder, which exhibits a volatile and explosive nature. 	<ul style="list-style-type: none"> • The geometric features such as pores and struts are limited to macro-scale, which may not be suitable in most biomedical applications since open porous structures with micron-scale pores and struts are required for good biological performance. • Topological discrepancies between the as-designed and as-built scaffolds, reported in the indirect manufacturing of Mg scaffolds, result in different pore size and strut thickness, which substantially impact cell ingrowth and mechanical integrity.

as-cast and as-extruded counterparts 0.3–2 ml/cm²-day. Shuai et al. [130] employed SLM process to enhance the corrosion resistance of ZK60 for biodegradable implant application. The grain refinement, homogenized microstructure, and extended solid solution due to the rapid solidification during SLM process enhanced corrosion resistance of ZK60 alloy. Cu-containing Mg alloys (AZ61) are aimed to combine the benefits of biodegradation of Mg and antibacterial functions of Cu. However, their clinical application is restricted by fast degradation. He et al. [76] improved the degradation resistance of AZ61 using SLM process. Likewise, Xu et al. [70] improved biodegradation resistance of ZK30-Cu alloy,

through grain refinement owing to rapid solidification during SLM process. The SLM-processed Mg-Sn alloys exhibited finer grains in comparison to as-cast and as-rolled Mg-Sn alloys [87], which lead to an improved biodegradation resistance.

Bioceramics exhibit low mechanical strength, while Mg exhibits suitable mechanical strength but poor corrosion resistance. Thus, bioceramic reinforced Mg alloys can provide the combination of adequate mechanical strength and corrosion resistance. However, agglomeration of β -TCP in Mg matrix during conventional manufacturing processes inhibits successful fabrication of β -TCP/Mg alloy composites [131–133].

Table 2
Formation quality of the additively manufactured Mg-based biomaterials.

Ref	Material	Topology	Formation quality
Liu et al. 2017 [72]	Mg-Ca	Porous structure	75.4 - 81.52%
Shuai et al. 2017 [130]	ZK60	Cube	72.8 - 97.4%
Deng et al. 2017 [85]	ZK60/x β -TCP	Cube	88.5 - 98.8%
Liu et al. 2019 [145]	AZ61	Cuboid	99.4%
Wei et al. 2019 [75]	Mg-xZn	Cuboid	94.70 - 99.35%
He et al. 2017 [76]	AZ61	Cuboid	76 - 98%
Shuai et al. 2017 [81]	Mg-3Zn/xHA	Cuboid	95.5 - 97.9%
Wei et al. 2014 [63]	AZ91D	Cuboid	99.52%
Yang et al. 2016 [68]	Mg	Cube	no formation pores&cracks
Wei et al. 2015 [84]	ZK60	Cuboid	82.3 - 94.1%
Bär et al. 2019 [36]	WE43	Cuboid	>99.9%
Kopp et al. 2019 [178]	WE43	Cuboid	Geometrical discrepancy: 2.5% greater strut size and 3% lower porosity
Zumdick et al. 2019 [74]	WE43	Cube	microscopic porosity < 0.2%
Li et al. 2018 [88]	WE43	Diamond lattice porous scaffold	Geometrical discrepancy: As-built strut size: 420 μ m; design value = 400 μ m As-built porosity: 64%; design value = 67%.
Qin et al. 2019 [73]	Zn-xWE43	Diamond lattice porous scaffold	Relative density: >99.47 - 99.93% Geometrical discrepancy: As-built strut size: 562 μ m; design value 400 μ m. As-built geometrical porosity: 45%; design value 67%.

Hence, Deng et al. [134] aimed to employ SLM process to prepare the composites of β -tricalcium phosphate (β -TCP) and Mg-6Zn-1Zr (ZK60). Rapid solidification allowed a homogeneous distribution of β -TCP along grain boundaries of α -Mg that promoted the formation of apatite film on the surface, thus hindered corrosion. Also, ZK60/8 β -TCP composite possessed improved mechanical strength and cytocompatibility. Shuai et al. [135] incorporated Nd into ZK60 alloy via SLM process. Fine α -Mg grains and intermetallic phases along the grain boundaries were observed in the as-built sample. Degradation resistance was improved with the formation of a dense surface layer promoted by the presence of Nd₂O₃, as well as the 3D honeycomb structure of intermetallic phases, which formed a tight barrier to inhibit corrosion.

In addition to grain size, intermetallic phase is also an important factor affecting the biodegradation behavior of Mg alloys [136,137]. Shuai et al. [138] studied different grain size and intermetallic phase volume fraction by introducing varying concentrations of Al into Mg-Zn alloy. ZK30-xAl cubes (5 mm \times 5 mm \times 5 mm) were fabricated via SLM. According to the results, grain size refined and fraction of intermetallic phase volume increased with Al content. When Al content was below 3 wt%, the grain refinement was the major factor affecting the degradation behavior. The finer grain created numerous grain boundaries, making the alloy passivate readily and lead to an improved degradation resistance. However, with Al further increasing, the intermetallic phase became the main factor affecting the degradation behavior even though grain size was further refined. In another study, Yang et al. [139] incorporated mesoporous silica into ZK60 alloy to improve the degradation resistance via SLM process. Owing to the fast heating and cooling during SLM process, mesoporous silica particles homogeneously distributed inside Mg matrix and formed a decent interface binding. Having a more posi-

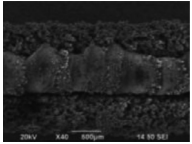
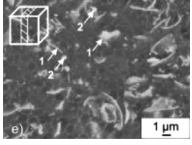
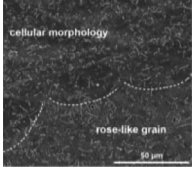
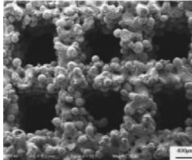
tive corrosion potential, mesoporous silica served for surface passivation of the Mg matrix. Also, the mesoporous structure and exceptional bioactivity of silica promoted the deposition of apatite layer, which served as a protection film against corrosion of Mg matrix.

The available literature on the biodegradation performance of additively manufactured Mg is summarized in Table 4. Improved microstructure, owing to the fast cooling and rapid solidification in SLM process, leads to enhanced biodegradation resistance.

3.4. Mechanical properties

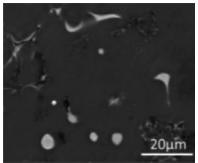
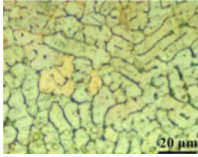
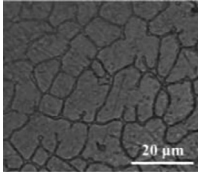
Implants and scaffolds should endure anatomic loads [46]. Therefore, their mechanical properties such as hardness, compressive and tensile strength, elasticity of stiffness, ductility, and toughness need to be analyzed before clinical applications. A significant mismatch between the elastic moduli of an implant/scaffold and the surrounding tissue can cause the so-called stress shielding, which occurs when the physical stresses are taken up by the implant rather than by the bone. Stress shielding causes bone atrophy that result in the loosening of implant/scaffold and eventually the premature failure of the implant/scaffold. The elastic modulus of cancellous and cortical bones are in the range of 22.4 – 132.3 MPa and 7.7 - 21.8 GPa, respectively. Implants/scaffolds should exhibit an elastic modulus mimicking that of natural human bone [140]. Thus, adjusting the elastic modulus to a right value is essential for implant/scaffold design. In that sense, several approaches can be used to prevent mismatch of mechanical properties between the implant/scaffold and bone. Alloying with β stabilizers is one of the approaches to reduce the elastic moduli of the implant/scaffold through the introduction of a β phase in the microstructure. Elastic moduli can

Table 3
Microstructural characteristics of the additively manufactured Mg.

Ref	Material	Microstructure					Micrograph
		Grain size (μm)	Phase identification	Remarks	Enhancement mechanism		
Ng et al. 2011 [125]	Mg	2.3 - 4.9	α -Mg	fine equiaxed grains of the α -Mg phase	The microstructure evolution was explained in terms of high cooling rate and rapid solidification during SLM.		
Zumdick et al. 2019 [74]	WE43	0.4 - 2.9; counterparts: 44.3	–	flake-shaped secondary phases (Mg ₃ Gd, Mg ₃ Nd, and Y ₂ O ₃) precipitated on the grain boundaries	Repeated cycles of rapid heating and cooling during SLM process lead to improved microstructure.		
Li et al. 2018 [88]	WE43	≤ 5	–	At the bottom of the struts rose-like grains At the top of the struts; cellular morphology	High cooling rates involved in SLM resulted in much finer grains than those achievable with conventional methods. Laser melting caused temperature gradients in the melt pool that contributed to the formation of strong marangoni convection and resulted in homogenous dispersion of alloying elements within the melt pool.		
Liu et al. 2017 [72]	Mg-Ca alloy	5 – 30	α -Mg & MgO	–	Grain refinement.		

(continued on next page)

Table 3 (continued)

Ref	Material	Microstructure				
		Grain size (μm)	Phase identification	Remarks	Enhancement mechanism	Micrograph
Chen et al. 2016 [71]	Mg-xZn	15 - 20	Mg matrix and a small amount of the second phase	–	The time for grain growth was very short due to rapid laser melting/solidification, which contributed to grain refinement. Presence of the second-phase hindered the growth of grains.	
Shuai et al. 2017 [87]	Mg-5Sn-xZn	Mg-5Sn: 15 Mg-5Sn-xZn: 5 - 11	–	–	Grain refinement of the alloys with increasing Zn content due to the increased number of nucleation particles in the process of solidification.	
Shuai et al. 2017 [81]	Mg-3Zn/xHA	Mg-3Zn: 16 Mg-3Zn/xHA: 6 - 11	–	Mg-3Zn: dendritic structure	During the laser process, the HA particles did not have enough time to accumulate in the melt pools with the rapid solidification rate, which contributed to the homogeneous distribution of HA and grain refinement.	

(continued on next page)

Table 3 (continued)

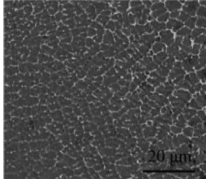
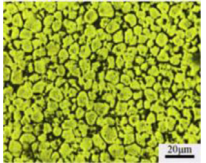
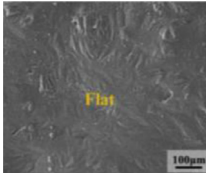
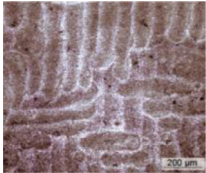
Ref	Material	Microstructure					Micrograph
		Grain size (μm)	Phase identification	Remarks	Enhancement mechanism		
Shuai et al. 2017 [130]	ZK60	6	α -Mg & Mg ₇ Zn ₃	Orderly dispersed grains with equiaxed structure	High densification, grain refinement, homogenized microstructure, and extended solid solution.		
Xu et al. 2019 [70]	ZK30-xCu	10; As-cast counterpart: 150	Mg, MgZn ₂ , and MgZnCu	–	–		
Liu et al. 2019 [145]	AZ61	1.61 – 2.46; as-cast counterpart: 200–300	α -Mg & β -Mg ₁₇ Al ₁₂	–	Enhanced solid solution.		
Wei et al. 2014 [63]	AZ91D	1.2; die-cast counterpart: 57	α -Mg, β -Mg ₁₇ Al ₁₂ , and a lesser degree of Al ₈ Mn ₅	–	–		

Table 4
Biodegradation performance of the additively manufactured biodegradable Mg parts.

Ref	Material	Geometry	Biodegradation
Shuai et al. 2017 [130]	ZK60	Non-porous block	Hydrogen evolution rate in Hank's solution: 0.006 - 0.019 ml cm ⁻² h ⁻¹
Xu et al. 2019 [70]	ZK30-xCu	Non-porous block	Biodegradation rate: ZK30 < ZK30-0.1Cu < ZK30-0.2Cu < ZK30-0.3Cu
Shuai et al. 2018 [16]	ZK60-xCu	Non-porous block	pH in SBF: ZK60: 9.3; ZK60-xCu: 9.5 – 11.3
Shuai et al. 2017 [135]	ZK60-xNd	Non-porous block	pH in SBF: ZK60: 9.52; ZK60-xNd: 8.6 – 12.2
Deng et al. 2017 [134]	ZK60/xβ-TCP	Non-porous block	pH in SBF: 9.4 - 10.7 Corrosion rate: 0.58 - 2.14 mm/year
Shuai et al. 2017 [87]	Mg-5Sn-xZn	Non-porous block	Hydrogen evolution rate in SBF: Mg-5Sn > Mg-5Sn-2Zn > Mg-5Sn-4Zn > Mg-5Sn-6Zn
Chen et al. 2016 [71]	Mg-xZn	Non-porous block	Hydrogen evolution: Mg-6Zn < Mg-2Zn, Mg-4Zn, and Mg-8Zn
Shuai et al. 2017 [81]	Mg-3Zn/xHA	Non-porous block	Hydrogen evolution volume after immersion for 300 h: Mg-3Zn: 83 mL/cm ² Mg-3Zn/xHA: 50 – 60 mL/cm ²
Liu et al. 2017 [77]	Mg-6Al-1Zn-xY	Non-porous block	The hydrogen evolution volume after immersion for 360: 6.1 - 30.1 mL/cm ² ·h AZ61 magnesium alloy with 2wt% Y exhibited the lowest degradation rate (0.28 mm/year)
Li et al. 2018 [88]	WE43	Diamond lattice porous cylinder; pore size: 600 μm	Satisfactory biodegradation behavior with around 20% volume loss after 4 weeks
He et al. 2017 [76]	AZ61	Non-porous block	Biodegradation rate: 1.2 - 2.4 mm/year after 24 - 144 h of immersion
Shuai et al. 2018 [93]	PHBV-xnMgO	Porous scaffold cylinder; pore size: 400 μm	Mass loss of the PHBV/5% nMgO scaffolds in PBS was double that of PHBV. After 35 days of immersion, the pH for the PHBV and PHBV/5% nMgO scaffolds were 6.85 and 7.63.
Sun et al. 2016 [94]	Mg ₂ SiO ₄ /x-CaSiO ₃	Porous scaffold Cuboid; Pore size: 500–800 μm	Scaffolds exhibited an improved degradability when CaSiO ₃ was introduced.

also be effectively reduced with porosity. According to the model of Gibson and Ashby [141], relative density is the most important structural characteristic of a porous material that influences Young's modulus. Relative density is the ratio of the density of the porous material (ρ) to that of the solid material (ρ_s). The relationships among the elastic modulus, plastic collapse strength, and relative density is defined by the following formulas:

$$\sigma_{pl} = 0.3(\rho/\rho_s)^{1.5}\rho_{ys} \quad (2)$$

$$E = (\rho/\rho_s)^2 E_s \quad (3)$$

where σ_{pl} is the plastic collapse strength, ρ/ρ_s is relative density, ρ_{ys} is yield strength. E represent the Young's modulus; subscript (s) represents the substrate material property. These equations describe that increasing porosity reduces the elastic modulus and plastic collapse strength. On the other hand, mechanical strength of an implant/scaffold can be improved through grain refinement according to the Hall–Petch equation as follows [142];

$$\sigma_y = \sigma_0 + \frac{K}{\sqrt{d}} \quad (4)$$

where σ_y is yield stress, σ_0 is a material constant for the starting stress for dislocation movement, K is another material constant; so-called strengthening coefficient, and d is grain size. In a similar way, the grain refinement significantly improves the hardness of the materials according to the

Hall–Petch equation as follows [142];

$$H = H_0 + \frac{k}{\sqrt{d}} \quad (5)$$

where H is the hardness of the material, H_0 and k are appropriate constants associated with the material hardness, and d is the grain size.

As mentioned before, SLM-produced materials possess refined grains due to high cooling rates and rapid solidification. Researchers studied manufacturing of biodegradable Mg alloys of different compositions using SLM. In the study of Ng et al. [143], single track of pure Mg showed grain refinement and enhanced hardness in accordance with the Hall–Petch equation. Yang et al. [68] built cubes of pure Mg through SLM process and confirmed the same enhancement mechanism. Later, variety of Mg alloys were built by SLM and exhibited improved hardness owing to the high cooling rates and rapid solidification [16,71,72,87,144,145].

Mechanical properties such as compressive strength, tensile strength, yield strength, and elastic modulus of the SLM produced Mg samples outperformed traditionally produced counterparts and favored orthopedic applications. Researchers agreed that grain refinement improves the hardness of the biodegradable Mg parts in accordance with the Hall–Petch equation. The hardness of the SLM produced Mg ranged from 0.4 to 1.2 GPa. The recent literature on the mechanical properties of additively manufactured Mg biomaterials is summarized in Table 5.

Table 5
Mechanical properties of the additively manufactured biodegradable Mg.

Ref	Material	Dimensions	Mechanical Properties	Enhancement mechanism
Ng et al. 2011 [125]	Mg	single track - 20 mm	Hardness: 0.59 - 0.87 GPa Elastic modulus: 21–33 GPa	Grain refinement improved hardness in accordance with the Hall–Petch equation.
Yang et al. 2016 [68]	Mg	Cubic $6 \times 6 \times 6 \text{ mm}^3$	Hardness: 42.9 - 48.3 Hv; powder-metallurgy-processed counterpart: 35 Hv	Grain refinement by laser rapid solidification favors improved hardness of SLM processed magnesium parts.
Chen et al. 2016 [71]	Mg-xZn	Cuboid $5 \times 5 \times 3 \text{ mm}^3$	Hardness: 62 - 71.5 Hv	Grain refinement due to the presence of the Mg-Zn phase and rapid solidification improved mechanical properties.
Wei et al. 2019 [75]	Mg-xZn	Cuboid $8 \times 8 \times 2 \text{ mm}^3$	Microhardness: 50 - 80 Hv; as-cast counterpart: 39 Hv UTS: 45 - 148 MPa; as-cast counterpart: 102 - 188 MPa elongation: 1.4% - 11.0%; as-cast counterpart: 7 - 18%	–
Shuai et al. 2017 [81]	Mg-3Zn/xHA	Cuboid $10 \times 10 \times 5 \text{ mm}^3$	Hardness: Mg-3Zn: 62 Hv as-extruded Mg-3Zn: 55 Hv hardness of Mg-3Zn/xHA composites was higher than that of Mg-3Zn alloy	The grain refinement enhanced hardness in accordance with the Hall–Petch equation.
Shuai et al. 2017 [130]	ZK60	Cube $6 \times 6 \times 6 \text{ mm}^3$	Microhardness: 70.1 - 89.2 Hv	High densification, grain refinement, homogenized microstructure, and extended solid solution.
Shuai et al. 2017 [135]	ZK60-Nd	Cube $8 \times 8 \times 8 \text{ mm}^3$	Compressive strength: 138.3 - 183.4 MPa Microhardness: 85.4 - 124.8 Hv	Enhanced microhardness is due to the solid solution strengthening, fine grain strengthening, and precipitation strengthening.
Shuai et al. 2018 [16]	ZK60-xCu ($x=0, 0.2, 0.4, 0.6$ and $0.8 \text{ wt}\%$)	–	compressive strength: SLM produced ZK60: 131.6 MPa SLM produced ZK60–0.4Cu: 158.3 MPa as-cast ZK60: 100 - 120 MPa as-extruded ZK60: 167 - 211 MPa Hardness: ZK60: 80.5 Hv ZK60–0.8Cu: 105.2 Hv	Grain refinement and uniformly dispersed MgZnCu phase enhanced the compression strength. The increased hardness of alloys with Cu content was due to the grain refinement and the formation of MgZnCu intermetallic phase.
Xu et al. 2019 [70]	ZK30 ZK30–0.3Cu	–	Hardness: 80 - 98 Hv	Improved hardness was due to the strengthening of the MgZn ₂ and MgZnCu phases.

(continued on next page)

Table 5 (continued)

Ref	Material	Dimensions	Mechanical Properties	Enhancement mechanism
Zhang et al. 2018 [85]	ZK61	Porous cuboid $6 \times 6 \times 9 \text{ mm}^3$ Porosity: 30%	Microhardness: 57.7 - 106.8 Hv UCS: 16 - 51 MPa Elastic modulus: 0.53 - 0.91 GPa	Microhardness enhancement is due to fine grain strengthening, solution strengthening and precipitation strengthening of second phases.
Shuai et al. 2017 [87]	Mg-5Sn-xZn ($x=0, 2, 4,$ 6 and 8 wt%)	Cuboid $10 \times 10 \times 3 \text{ mm}^3$	The hardness of the alloys increased with increasing Zn content.	The increase of the hardness was due to the grain refinement strengthening and the solid solution strengthening.
Liu et al. 2017 [77]	Mg-6Al-1Zn	Cuboid $10 \times 10 \times 5 \text{ mm}^3$	The hardness of AZ61: 90.9 Hv. The hardness increased as Y increased from 0wt% to 2wt%	Improved hardness is due to second phase strengthening.
Liu et al. 2019 [145]	Mg-6Al-1Zn-xY AZ61	Cuboid $10 \times 10 \times 7 \text{ mm}^3$	UTS: 239 – 287 MPa; as-cast counterpart: 140 MPa $\sigma_{0.2}$: 217 – 233 MPa; as-cast counterpart: 99 MPa %elongation: 2.1 – 3.3%; as-cast counterpart: 5.2%	–
He et al. 2017 [76]	AZ61	Cuboid $10 \times 10 \times 5 \text{ mm}^3$	Microhardness: 93 Hv	Grain refinement significantly improved the mechanical properties.
Wei et al. 2014 [63]	AZ91D	Cuboid $10 \times 10 \times 5 \text{ mm}^3$	UTS and yield strength ($\sigma_{0.2}$) of the SLMed samples are superior to those of the die-cast AZ91D UTS: 274 - 296 MPa, $\sigma_{0.2}$: 237 - 254 MPa microhardness: 85 - 100 HV; die-cast ingot counterpart: 58 Hv	Grain refinement improved microhardness.
Zumdick et al. 2019 [74]	WE43	Cube $12 \times 12 \times 12 \text{ mm}^3$	elastic modulus: 45.7 GPa UTS: 308 MPa mean lower yield: 296.3 MPa elongation: 5 - 6% elongation at fracture: 12% - 22%	Repeated cycles of rapid heating and cooling during SLM process improved mechanical properties.
Qin et al. 2019 [73]	Zn-xWE43 ($x: 0, 2, 5,$ 8wt%)	Diamond lattice Porous scaffold cubes of $5 \times 5 \times 10 \text{ mm}^3$ strut size: 400 μm pore size: 600 μm design porosity: 67%	Hardness: Zn: 42 Hv Zn-WE43: 114 – 169 Hv yield strength: Zn: 114 Mpa Zn-WE43: 154 – 335 MPa elongation after break: Zn: 10.1% Zn-WE43: 0.9 - 1.8%	Ductility decreased with WE43 content.
Shuai et al. 2018 [93]	PHBV-nMgO	Porous scaffold cylinder; d: 12.7 mm, h: 25.4 mm pore size: 400 μm	compressive strength: 2.62 - 5.14 MPa; human trabecular bone: 4 - 12 MPa compressive modulus: 29.33 – 44.68 MPa; human trabecular bone: 50 to 500 Mpa	The significant improvements were resulted from strong reinforcing effects of MgO nanoparticles.

3.5. Topology design

Human bone tissues are two types: cortical and cancellous. Cortical bone, also called compact bone, is the hard outer layer of bones with low porosity, while cancellous bone, also called trabecular bone, is the internal tissue of the skeletal bone with an open cell porous network and is much lighter than cortical bone. The porosity of cancellous bone is in the range of 30% - 95% and the pore size ranges from 200 to 1000 μm . Porous scaffolds are designed to mimic human bone structure. The delicate pores allow for new tissue ingrowth and body fluid circulation. Moreover, the porous scaffolds can provide the necessary support for cells to proliferate and maintain their differentiated functions, and their structure defines the ultimate shape of the new bone [140]. The formation and regeneration of new tissues are enabled by the biologic activities such as the attachment and proliferation of the cells. Thus, a well-designed porous structure is necessary for a decent biologic function. Porosity can also be used to adjust the mechanical properties of the designed structures, such as the strength and Young's modulus.

In the AM of a biomedical implant or scaffold, the patient's own bone is scanned before the model design. To this end, different scanning methods such as magnetic resonance imaging (MRI) and X-ray computed tomography (CT) can be used to collect an accurate image data [62]. This data is corrected by using a biomaterial software such as Biobuild[®] (Anatomics, Australia) or Mimics[®] (materialise, Belgium) and transferred to 3D CAD models. After the design is complete, the model is materialized via AM processes. In addition to the anatomical shape of the patient, scaffolds should be designed in a porous structure to mimic human bone tissue. The intricate pores inside the scaffold promote tissue ingrowth by providing pathways for effective diffusion of nutrients and oxygen to the cells and excretion of waste from the cells. Moreover, the biodegradation rate of the scaffolds is significantly influenced by porosity due to the change in the surface area [140].

The influence of geometric features on biological and mechanical properties is interrelated and needs to be well-understood [28]. For example, an increase in porosity can lead to better cell ingrowth but at the cost of poor stiffness, strength, and corrosion resistance [14,20,146,147]. Thus, the biodegradable scaffolds should be carefully designed and manufactured with customized geometry and porosity to meet the multiple requirements such as sufficient stiffness and permeability for a decent mechanical and biological function [148]. In this regard, finding the optimal topologies for scaffolds is of critical importance. Topology optimization is a design method that provides optimal geometry to achieve multiple goals such as maximum stiffness and strength with specific porosity under the given boundary conditions. Eventually, the optimal unit cell is designed, and based on that, the final periodical architecture is attained to meet the predefined design goals. Dong-ming et al. [148] employed topology optimization to achieve a microstructure with maximum stiffness under the constraint of specific pore volume fraction. In the study, algorithms and programs were built to obtain 2D

and 3D optimized microstructure, then they were converted to CAD models. The 3D geometry and pore shape in the metallic scaffolds were relatively precisely reproduced at a minimum mean pore size of 231 μm . Arabnejad et al. [118] identified the design limits of different lattice structures fabricated by SLM process by taking into consideration of the bone ingrowth requirements (i.e. pore size and porosity), mechanical function, and manufacturing limitations (i.e. strut thickness). Similar strategies can be applied to obtain design limits of other unit cell topologies and other manufacturing methods.

Porosity is defined as the percentage of void space in a solid structure, and the gravimetric method is used to calculate the porosity (P) as follows;

$$P = (1 - \rho_{\text{structure}}/\rho_{\text{material}}) \times 100 \quad (6)$$

where ρ_{material} and $\rho_{\text{structure}}$ are the density of raw material and porous structure, respectively.

In natural tissues, minimum distance of cells to the nearest capillary is 200 μm , which is the effective diffusion distance of oxygen and nutrients [149]. Thus, a scaffold should be designed with a minimum pore size of a few hundred micrometers for the delivery of oxygen and nutrients to the cells [150]. In the literature, the mostly used pore size varies between 100 and 500 μm [151–155]. Quantity of cells that can penetrate and grow in scaffold, as well as the amount of biofunctions that can be transported through the scaffold depend on the size and interconnectivity of pores [156]. Therefore, a porous structure with small pore size and poor interconnectivity may not provide sufficient space for bone ingrowth, and permeability for material transport through the scaffold. Interconnectivity of pores is also essential for the matrix deposition and vascularization [156]. Besides the porosity and pore size, other geometrical features such as the surface curvature and pore shape have also significant influence on the cellular response and tissue regeneration [157]. It has been reported that tissue regeneration occurs preferentially on concave surfaces rather than convex and planar surfaces [158–160], and the rate of tissue regeneration improves with curvature [161–163].

3.6. Process parameters

The properties of the additively manufactured scaffolds strongly depend on process parameters, such as laser spot diameter, input power, scanning speed, hatch spacing, and layer thickness [152,164–166]. Therefore, understanding the effects of these parameters during the building process and selection of the optimal conditions can allow attaining near full density parts. The range of suitable processing parameters is also dependent on the chemical composition of the primary alloys [167]. Generally, it has been reported that an optimal laser energy density is required to produce parts with maximum density [168,169]. The optimal energy density can be set by adjusting the laser power, scan speed, hatch spacing, and layer thickness [170], based on the following formula:

$$E_v = \frac{P}{v \cdot H \cdot T} \quad (\text{J}/\text{mm}^3) \quad (7)$$

where E_v is the energy density (J/mm^3), P is laser power (W), v is scanning speed (mm/s), H is hatch spacing (mm), and T is layer thickness (mm). Manufacturing of denser parts can be achieved at reduced scanning speeds since it permits longer interaction time between powder and laser beam, which increases energy delivery rate to the powder bed [170]. At high scanning speeds less energy is transferred to the powder that may cause incomplete melting of particles and formation of pores inside the struts. Delivering sufficient energy to the powder bed enables adequate melting of particles to fully infiltrate into the voids to form a highly dense structure. Optimizing the process parameters is conducive to enhanced melt pools and favorable material densification. Energy density is an essential parameter in controlling defects and improving mechanical properties [171]. In the literature, various studies on the optimization of process parameters for AM of Mg have been reported [172,173]. Niu et al. [128] identified that the laser-introduced defects in SLM processed Mg initiated localized corrosion and reduced the overall corrosion resistance. The study suggested that these volume defects and the subsequent corrosion can be reduced by selecting suitable combination of the process parameters. Ng et al. [125] investigated the interaction between the laser source of SLM and the Mg powders by varying the laser power and scan speed under continuous and pulse wave irradiation modes. The required energy density range for continuous and pulse wave irradiation was determined as $1.27 \times 10^9 - 7.84 \times 10^{12} \text{ J}/\text{m}^2$ and $1.13 \times 10^{12} - 9.8 \times 10^{12} \text{ J}/\text{m}^2$, respectively. Higher peak power under pulse wave irradiation required higher energy density in comparison to continuous wave irradiation. The surface morphology and dimension characteristics of the Mg specimens varied under different laser irradiation modes. Under continuous wave irradiation, disrupted surface and smooth regular beads were formed. Though, under pulsed wave irradiation relatively smooth and flat surface morphology was observed [143]. Yang et al. [68] also studied the influence of laser energy density on the formation quality of Mg parts. They achieved continuous smooth Mg layers, without the presence of formation pores and cracks at input laser power of 50–80 W, scanning speed of 300–700 mm/min, and a corresponding laser energy density of 6.0–12.0 J/mm. Sufficient energy density permitted total melting of solid Mg particles into liquid phase. Rapid solidification of the Mg melt lead to finer grains and formation of continuous smooth layers. Shuai et al. [130] studied the effect of SLM process parameters on the properties of as-built ZK60 alloys. Alloy samples with relative density of 97.3% was obtained at an energy density of $600 \text{ J}/\text{mm}^3$. High scanning speed and low energy density resulted in formation pores due to incomplete melting and high liquid viscosity, while low scanning speed caused formation of micro cracks, due to severe thermal stresses.

He et al. [76] achieved fabrication of AZ61 alloy with a relative density of 98%. Input laser power of 60–90 W was identified as the forming zone of AZ61. An increase of the laser power was found useful for enhancing degradation resistance and microhardness due to the improved densification and formation of uniformed equi-axed grains. However, ex-

cessive laser power lead to an increased mass loss and reduced microhardness due to coarsening of grains and a reduction in the solid solution of Al in the Mg matrix. Liu et al. [145] investigated the effect of process parameters on the properties of AZ61 manufactured by SLM. According to the results, applied laser energy density significantly affected the relative density, surface topography, and microstructure of the as-built samples. The relative density reached maximum 99.4% at a laser energy density $156.3 \text{ J}/\text{mm}^3$ and scanning speed 400 mm/s. In addition, the optimal hatch spacing for highest relative density and surface quality was determined to be 0.06 mm. Pawlak et al. [174] adopted the design of experiments approach to study the influence of process parameters and their correlations, as well as the minimization of processing pores on SLM processed AZ31 through optimization. They developed a mathematical model, which provided a very good estimate of porosity values. Optimization allowed to fabricate AZ31 alloys with relative density above 99.5% using SLM process.

Ji et al. [175] developed an analytical model to predict the post-printing grain size in metal AM. According to the study, the temperature at top surface of the build part is not affected by the scan speed, while both the affected zone and peak value of the temperature beneath the surface of the build part increase with the increase of the laser power. The average grain size decreases with the increase of the laser power, while the average grain size decreases with the increase of the scan speed and then increases due to the incomplete melting effect. Thus, the study concluded that the selection of proper laser parameters is very important in controlling the post-printing grain size, so the mechanical properties of the build part. Yang et al. [139] incorporated mesoporous silica (MS) with ZK 60 alloy by SLM with optimal processing parameters; laser spot size $50 \mu\text{m}$, input power 120 W, scanning speed $20 \text{ mm}\cdot\text{s}^{-1}$, hatch spacing $40 \mu\text{m}$, and layer thickness $100 \mu\text{m}$. A high densification $98.3 \pm 0.8\%$ was achieved with ZK60, which was slightly reduced with the addition of mesoporous silica; $97.2 \pm 1.4\%$ for ZK60/4MS and $96.4 \pm 2.4\%$ for ZK60/8MS. Reduced densification was attributed to the high melting point of silica, which remained un-melted while ZK60 fully melted into liquid phase and infiltrated most voids that lead to high densification.

The literature on the applied process parameters for AM of biodegradable Mg is summarized in Table 6. The laser power is the mostly investigated input parameter, which ranged from 20 to 200 W. A broad range of laser scanning speeds was adopted for manufacturing of Mg-based biodegradable parts. Other parameters such as laser spot diameter, powder layer thickness, and hatch spacing was in a range of 50 – 150 μm , 20 – 200 μm , and 50 – 250 μm , respectively.

3.7. Powder properties

In addition to the process parameters, powder properties such as particle type, morphology, size and size distribution have significant influence on the properties of the additively manufactured Mg implants and scaffolds [152,164,165].

Table 6
Process parameters for the additive manufacturing of Mg.

Ref	Material	SLM Process Parameters				
		Laser Power (W)	Laser Spot Size (μm)	Scanning Speed (mm/s)	Layer Thickness (μm)	Hatch Spacing (μm)
Yang et al. 2016 [68]	Mg	20 – 100	50	1.7 – 15	100	–
Chen et al. 2016 [71]	Mg-xZn	70	50	100	100 - 200	–
Liu et al. 2019 [145]	AZ61	150	70	250 - 1800	40	60 - 100
He et al. 2017 [76]	AZ61	10 - 110	150	3.3	50	50
Wei et al. 2014 [63]	AZ91D	200	–	170 - 1000	40	70 - 130
Xu et al. 2019 [70]	ZK30	75	150	15	50	50
Wei et al. 2015 [84]	ZK60	200	150	100 – 900	20	80
Shuai et al. 2018 [16]	ZK60-xCu	60	150	10	–	100
Shuai et al. 2017 [135]	ZK60-xNd	60	150	7.5	100	100
Zhang et al. 2018 [85]	ZK61	60 - 110	100	–	40	1500
Gangireddy et al. 2019 [37]	WE43	135 – 195	100	800 – 1200	30	200 - 250
Zumdick et al. 2019 [74]	WE43	200	125	700	30	40
Bär et al. 2019 [36]	WE43	200	125	700	30	40
Qin et al. 2019 [73]	Zn-xWE43	70	75	500	30	70

Flowability of the powder greatly depends on the size and size distribution, and morphology of particles. Spherical particles with narrow size distribution allow for enhanced powder flow that in turn improves packing of powders and eliminate formation defects. Thus, powders with suitable properties should be selected/prepared to obtain products of high relative density [58,134] and favorable mechanical and biological properties. In this context, the properties of the powder materials used in different researches for AM of Mg-based biomaterials are summarized in Table 7. Researchers mostly employed particles with spherical morphology and size smaller than $100\mu\text{m}$. Clinically validated WE43 powder is the mostly investigated Mg alloy, which was followed by ZK and AZ series Mg alloys.

3.8. Post-processing

Post-treatment of additively manufactured Mg implants and scaffolds is important to enhance the mechanical performance, to better mimic human tissue, and satisfy desired biologic functions. The microstructure of additively manufactured materials differs from that of the materials manufactured by subtractive methods [20,176]. The layer-by-layer build-up process of AM with high cooling rates results in significant internal stresses in the built structure [20]. The undesired instabilities of the melt pool during PBF process may lead to increased porosity and surface roughness. Thus, post-processing is routinely applied to reduce the thermal stresses and to enhance the microstructure in order to meet the product requirements. The post-treatment technologies can be classified into two as heat treatment and surface treatment.

Heat treatment is an effective method to enhance the performance of an additively manufactured part by modifying its microstructure. Heat treatment also reduces the microstructural defects and residual thermal stress. In SLM, the powders fuse and form a molten pool under the scanning of

high-energy laser, thus completing the fully melting and re-solidification mechanism. However, the temperature distribution of the molten pool significantly varies at the inner and outer regions, resulting in different temperature gradients in different directions. As a result, the cooling rate in the molten pool differs in each direction, which leads to anisotropic microstructure in the built part. Also, there are re-melting areas present at each layer, which exhibits different microstructure in comparison to the regions without re-melting. SLM also involves very high cooling rates exceeding 10^5 K/s [68], which causes residual stress in the as-built parts. Residual stress can significantly reduce the ductility of scaffolds. Thus, heat treatment is necessary to reduce the microstructural anisotropy and to relieve the residual stress existing in the SLM processed materials [177].

Porous magnesium scaffold possesses a high surface area, which stresses the vast degradation and early loss of mechanical integrity of the scaffold and tissue, unless prevented by suitable post-processing methods. Kopp et al. [178] manufactured Mg scaffolds using SLM method and studied the influence of two different post-processing methods; heat treatment and plasma electrolytic oxidation (PEO) on the degradation behavior of the scaffold in vitro. PEO treatment reduced the degradation rate of magnesium scaffold, and enhanced its mechanical performance, whereas heat treatment showed a detrimental effect. Heat-treated samples revealed an increased precipitation of alloying elements at the grain boundaries, which resulted in a more selective corrosion attack of especially single grains. The heat treated sample exhibited higher corrosion penetration depths due to high amount of grain border excretions, which caused increased corrosion rates. Gangireddy et al. [37] manufactured WE43 Mg alloy using SLM process and applied HIP as a post-treatment. Although, HIP treatment effectively densified the samples of high initial porosities, its effect was insignificant at small porosity level due to the enclosed nature of the pores. Mechanical strength was highly

Table 7
Properties of powders used in additive manufacturing of biodegradable Mg.

Reference	Powder properties		
	Material	Size	Morphology
Yang et al., 2016 [68]	Mg	1 - 10 μm	spherical
Ng et al., 2011 [125]	Mg	45 μm	spherical
Bär et al., 2019 [36]	WE43	20 - 63 μm	–
Zumdick et al., 2019 [74]	WE43	25 - 63 μm	spherical and some elongated particles
Gangireddy et al., 2019 [37]	WE43	15 - 63 μm	–
Li et al., 2018 [88]	WE43	25–60 μm	Nearly spherical
Kopp et al., 2019 [178]	WE43	45.8 μm	–
Qin et al., 2019 [73]	Zn-xWE43	Zn: 15–45 μm WE43: 25 - 63 μm	spherical
Wei et al., 2015 [84]	ZK60	30 μm	spherical
Shuai et al., 2017 [130]	ZK60	50 μm	spherical
Shuai et al., 2018 [16]	ZK60-xCu	ZK60: 50 μm Cu: 80 μm	ZK60: spherical Cu: spherical
Shuai et al., 2017 [135]	ZK60-xNd	ZK60: 50 μm Nd: 10 μm	ZK60: Spherical Nd particles: Irregular shape
Deng et al., 2018 [85]	ZK60/ β -TCP	β -TCP: 200 nm ZK60: <50 μm	spherical
Zhang et al., 2018 [85]	ZK61	ZK61: 50 μm Zn: 5 μm - 30 μm	ZK61: spherical Zn: irregular shape
Wei et al., 2019 [75]	Mg-xZn	Mg: 32 μm Zn: 19 μm	Mg and Zn: near-spherical
Chen et al., 2016 [71]	Mg-xZn	–	spherical
Shuai et al., 2017 [81]	Mg-3Zn/xHA	HA: width: 20 nm, length: 150 nm Mg-3Zn: 60 μm	HA: needle-like shape Mg-3Zn: spherical
Shuai et al., 2017 [87]	Mg-5Sn-xZn	Mg: 10 μm Sn: 2 μm Zn: 2 μm	All spherical
Liu et al., 2019 [145]	AZ61	30 - 70 μm avr: 48 μm	spherical
He et al., 2017 [76]	AZ61	70 μm	spherical
Wei et al., 2014 [63]	AZ91D	59 μm	spherical
Liu et al., 2017 [77]	Mg-6Al-1Zn/xY	AZ61: 70 μm Y: 20 μm	AZ61: spherical Y: irregular-shaped
Liu et al., 2017 [72]	Mg-Ca	100 - 200 μm	spherical
Shuai et al., 2018 [93]	PHBV-xnMgO	PHBV: 1 μm nMgO: 50 nm	–
Vorndran et al., 2013 [108]	Mg ₃ (PO ₄) ₂	16 μm	–
Meininger et al., 2015 [109]	Mg ₃ (PO ₄) ₂ Mg _{2.5} Sr _{0.5} (PO ₄) ₂ Mg ₂ Sr ₁ (PO ₄) ₂	<355 μm	–
Sun et al., 2016 [94]	MgO-CaO-SiO ₂ (Mg ₂ SiO ₄ /x-CaSiO ₃)	Mg ₂ SiO ₄ : 5 μm CaSiO ₃ : 0.2–2 μm	Irregular shape

dependent on the inherent porosity of the samples, which substantially reduced with increasing porosity.

A smooth surface is critical to enhance corrosion resistance and prevent fatigue failure [28]. However, due to the attachment of partially melt particles on the surface of as-built Mg parts during SLM process, surface modification is required [28]. Surface roughness plays an important role in the interaction between scaffold and cells [28]. Thus, biological performance of additively manufactured scaffolds, particularly bioactivity and biocompatibility can be significantly enhanced by surface modification [20].

Surface modification can be achieved by various techniques such as plasma spray, physical or chemical vapor deposition, ion implantation, electrochemical oxidation, acidic or alkali etching, sol-gel, heat-treatment, and surface machining or grinding. For porous metallic structures, there are two main approaches, based on surface coating and surface corrosion [20]. Corrosion-based surface treatment involves interfacial chemical reactions of structures in corrosive solution. Such chemical processes include chemical etching and anodization treatments. On the other hand, coating bioactive ceramics on scaffold surface is considered an effective way to improve the surface bioactivity of scaffolds [177].

4. Challenges of additive manufacturing of biodegradable Mg

The Powder Bed Fusion (PBF) of Mg-based metal powders holds two major challenges; vigorous evaporation and high chemical reactivity [37,74,84,179]. The vigorous evaporation of Mg powders is due to its low boiling point. The temperature gap between the melting and boiling point of Fe and Ti is about 1300 K and 1600 K, respectively, whereas this gap is less than 500 K for Mg [28,64]. Therefore, the evaporation tendency of Mg is very high during SLM process [180,181]. Wei et al. [84] studied evaporation of ZK60 during SLM process. Both Mg and Zn are volatile elements, and diffusivity of the vaporized Zn is higher than vaporized Mg in argon atmosphere. Thus, higher Mg:Zn ratio and a lower content of Mg and Zn than the raw material was reported with a refined microstructure and reduced Mg–Zn precipitates. The relative density was reported to be limited to 94%. Negative effects of evaporation during SLM processing of Zn-WE43 was eliminated by Qin et al. [73]. They adopted a customized gas circulation system and optimized the laser energy input. They achieved above 99% relative density.

Mg is very reactive to oxygen even in its bulk form. The powder form of Mg used in SLM greatly increases the surface area, which can easily cause a strong exothermic reaction and serious dust explosions [28,74,88,182]. Therefore, most laboratories avoid AM of Mg due to safety concerns [183]. Thus, it is recommended to passivate Mg powders by oxidation during atomization to ensure safe handling. Sometimes, Mg powders are even atomized under argon atmosphere in mixture with 1–2% oxygen, which forms a relatively stable oxide layer on Mg powders. However, oxygen in the Mg powder has a negative effect on SLM process [28]. The melting point of MgO is 2852 °C, which is significantly higher than that of Mg and its alloys. More laser energy is required to melt the oxide layer, which in turn worsens evaporation due to the increased temperature in the molten pool. As a consequence, the formation quality deteriorates with increased processing pores and inclusions [28,184]. Also, the presence of a surface oxide film on the preceding layer inhibits interlayer bonding due to the poor wettability of oxide films by liquid metals, which results in balling [17,64]. Occurrence of balling region is characterized by the agglomeration of a series of ball like particles, where the liquid phase splits into a row of spheres to reduce surface energy to form big melt pools [170]. Incidence of balling lead to deterioration of the surface features resulting from the combination of thermal stresses and weak interlayer bonding between grains and layers [17].

Despite the extremely low oxygen content in the high purity shielding Ar gas, Mg powder oxidizes during SLM process. Salehi et al. [64] investigated interaction of Mg powder with an ultra-high purity (99.9999%) Ar gas using the thermogravimetric analysis (TGA) technique at different heating rates (5, 10, 15, 20, 22.5, 25, and 28 °C/min). The results showed that Mg powder reacts with even a very low oxygen content present as impurity in the Ar gas to form MgO at temperatures higher than 400 °C. Thus, high purity Ar gas only provides inert atmosphere for Mg powder below 400 °C. For temperatures exceeding 400 °C, Mg powder significantly reacts with oxygen present as an impurity in ultra-high purity Ar gas to form MgO. With increasing heating rate, the onset of oxidation progressively shifted to higher temperatures. Oxidation reactions of Mg powder under Ar atmosphere was described by two different oxidation mechanisms, namely, the oxide thickening and sublimation/vaporization of Mg.

During SLM process, due to the low absorption of magnesium, major portion of the laser energy is reflected. Research should be conducted to assure that majority of energy is delivered to the material to achieve higher efficiencies. Another important consideration is that the evaporation fume emitted during SLM of Mg should be carefully blown off through a continuous gas flow. Also, a special care should be taken to prevent the disturbance of the very light-weight Mg powder bed from the continuous flow of the shielding gas [28].

It should also be noted that solidification cracks may occur during SLM processing of base materials of brittle nature. Rapid heating and cooling of brittle metal powder in SLM process will lead to residual stress that will result in

cracks in the as-built parts. Therefore, brittle powders should be avoided for SLM fabrication. In addition, SLM-built parts usually exhibit a rough surface due to the attachment of the partially melted particles during SLM process that can deteriorate the mechanical properties such as the fatigue strength. Thus, post treatments are necessary to improve the surface quality of the SLM-produced Mg parts [140].

5. Concluding remarks and future research

AM is the right method to produce Mg-based implants and porous scaffolds with customized structures based on the patient specific anatomic data. Among the AM processes, Powder Bed Fusion (PBF) is the most suitable one, which allows for a precise control over the topology. The processes other than PBF employ sacrificial materials, such as binders for binder jetting and polymeric templates for infiltration (indirect AM), which cause the waste of additional materials and lead to poor densification. Though recent studies suggest the possibility of eliminating the sacrificial materials, as-built Mg parts still possess insufficient formation quality. EBM is considered not a suitable process since the severe evaporation of Mg affects the propagation of electron beam in vacuum inside the build chamber. SLM outperforms SLS process owing to the complete melting and effective infiltration of Mg, which leaves no voids in the bulk material/struts, leading to high densification. The high cooling rates and rapid solidification of SLM favors improved microstructure with refined grains, homogenized phase distribution, and enhanced solid solution. Thus, mechanical and corrosive performance of SLM produced Mg outperform that of traditionally produced counterparts. Powder properties and processing conditions significantly affect the formation quality, dimensional accuracy, microstructure, biological and mechanical functions of the as-built Mg implants and scaffolds. The optimal powder properties and processing conditions permit to achieve higher material densification and energy efficiency. In this regard, literature lacks studies investigating the effect of varying powder properties and process conditions on the energy efficiency of SLM process for the fabrication of Mg parts. Attachment, proliferation, and differentiation of new cells are significantly influenced by the topology design of the scaffolds. Limited effort has been put forth to investigate the AM of Mg with different lattice structures. Hence, more research is required to comparatively investigate the effect of different lattice structures, porosity, and pore topology in order to identify the ideal scaffold design for best performance. Biological performance of the as-built Mg may differ in vitro and in vivo. Despite the availability of in vitro studies, literature lacks investigation of the biodegradation performance of the additively manufactured Mg in vivo. Thus, researchers are encouraged to conduct in vivo studies on the biodegradation performance of the additively manufactured Mg implants and scaffolds. Finally, considering the healing period of the defected tissues, the influence of time (up to ~2 months) on the in vivo performance of the additively manufactured Mg implants and scaffolds should

be studied as a fourth dimension for the ultimate success of the implants and scaffolds in the clinical applications.

References

- [1] A. Paula, M. Madrid, A. Paola, S.M. Vrech, M.A. Sanchez, *Mater. Sci. Eng. C* 100 (2019) 631–644, doi:10.1016/j.msec.2019.03.037.
- [2] F. Witte, H. Ulrich, C. Palm, E. Willbold, *J. Biomed. Res. Part A* 81 (3) (2007) 757–765, doi:10.1002/jbm.a.
- [3] N. Kleer, et al., *Materialia* 8 (2019) 100436 August, doi:10.1016/j.mtla.2019.100436.
- [4] D. Zamani, F. Moztafzadeh, D. Bizari, *Int. J. Biol. Macromol.* 137 (2019) 1256–1267, doi:10.1016/j.ijbiomac.2019.06.182.
- [5] C. Shuai, S. Li, S. Peng, P. Feng, Y. Lai, C. Gao, *Mater. Chem. Front* 3 (2019) 544–562, doi:10.1039/c8qm00507a.
- [6] E. Nazarzadeh, M. Mansour, M. Mohseni, *Synth. Met.* 187 (2014) 9–16, doi:10.1016/j.synthmet.2013.09.045.
- [7] A. Chaya, et al., *Acta Biomater.* 18 (May 2015) 262–269, doi:10.1016/j.actbio.2015.02.010.
- [8] B. Wegener, et al., *Mater. Sci. Eng. B* 176 (20) (2011) 1789–1796, doi:10.1016/j.mseb.2011.04.017.
- [9] S. Han, et al., *Drug Deliv.* 10 (2012) 1596–1606, doi:10.1002/sml.201102280.
- [10] E. Marukawa, et al., *J. Biomed. Mater. Res. Part B Appl. Biomater.* 7 (104) (2016) 1282–1289, doi:10.1002/jbm.b.33470.
- [11] B.J. Kim, Y. Piao, M. Wufuer, W.C. Son, T.H. Choi, *J. Oral Maxillofac. Surg.* 5 (76) (2018) 1055–1060.
- [12] A. Torroni, C. Xiang, L. Witek, E.D. Rodriguez, P.G. Coelho, N. Gupta, *J. Cranio-Maxillofacial Surg.* 12 (45) (2017) 2075–2083.
- [13] M.P. Staiger, A.M. Pietak, J. Huadmai, G. Dias, *Biomaterials* 27 (2006) 1728–1734, doi:10.1016/j.biomaterials.2005.10.003.
- [14] X.P. Tan, Y.J. Tan, C.S.L. Chow, S.B. Tor, W.Y. Yeong, *Mater. Sci. Eng. C* 76 (2017) 1328–1343, doi:10.1016/j.msec.2017.02.094.
- [15] E. Dayaghi, et al., *Mater. Sci. Eng. C* 102 (2019) 53–65.
- [16] C. Shuai, L. Liu, M. Zhao, P. Feng, Y. Yang, W. Guo, *J. Mater. Sci. Technol.* 34 (2018) 1944–1952, doi:10.1016/j.jmst.2018.02.006.
- [17] V. Manakari, G. Parande, M. Gupta, *Metals (Basel)* 7 (2) (2017) 1–35, doi:10.3390/met7010002.
- [18] Y. Li, et al., *Acta Biomater.* 77 (2018) 380–393, doi:10.1016/j.actbio.2018.07.011.
- [19] P. Of, *I. Transport, Library (Lond)* 341 (26) (1999) 1986–1995, doi:10.1056/NEJM199912233412607.
- [20] X. Wang, et al., *Biomaterials* 83 (2016) 127–141, doi:10.1016/j.biomaterials.2016.01.012.
- [21] A.S. Prasad, *Mol. Med.* 14 (5–6) (2008) 353–357, doi:10.2119/2008-00033.Prasad.
- [22] H. Tapiero, K.D. Tew, *Biomed. Pharmacother.* 57 (9) (2003) 399–411, doi:10.1016/S0753-3322(03)00081-7.
- [23] K.M. Hambidge, N.F. Krebs, *J. Nutr.* 137 (4) (2007) 1101–1105, doi:10.1093/jn/137.4.1101.
- [24] G. Song, *Corros. Sci.* 49 (2007) 1696–1701, doi:10.1016/j.corsci.2007.01.001.
- [25] K. Hong, et al., *J. Mech. Behav. Biomed. Mater.* 98 (2019) 213–224.
- [26] T. Stodnitzky, B.I. Morgenthal, O. Andersen, C. Kostmann, F. Witte, B. Kieback, *Adv. Eng. Mater.* 16 (3) (2014) 309–318, doi:10.1002/adem.201300130.
- [27] C. Brandt-Wunderlich, et al., *J. Mech. Behav. Biomed. Mater.* 91 (2019) 174–181.
- [28] Y. Qin, et al., *Acta Biomater.* (2019) In press, doi:10.1016/j.actbio.2019.04.046.
- [29] S. Galli, et al., *JACC Cardiovasc. Interv.* 12 (4) (2019) S39, doi:10.1016/j.jcin.2019.01.140.
- [30] T. Kraus, et al., *Acta Biomater* 66 (2018) 109–117, doi:10.1016/j.actbio.2017.11.031.
- [31] T.T.T. Trang, et al., *Nat. Commun.* 9 (1) (2018), doi:10.1038/s41467-018-04981-4.
- [32] A. Dehghanghadikolaei, H. Ibrahim, A. Amerinatanzi, M. Elahinia, *Biodegradable Magnesium Alloys*, 2nd ed., Elsevier Ltd, 2019.
- [33] C.L. Mendis, K. Hono, *Understanding Precipitation Processes in Magnesium Alloys*, Woodhead Publishing Limited, 2013.
- [34] H. Westengen, *Encycl. Mater. Sci. Technol.* (2001) 4743–4744, doi:10.1016/b0-08-043152-6/00826-3.
- [35] R. Parai and S. Bandyopadhyay-Ghosh, “,” *J. Mech. Behav. Biomed. Mater.*
- [36] F. Bär, et al., *Acta Biomater.* (2019) In Press, doi:10.1016/j.actbio.2019.05.056.
- [37] S. Gangireddy, B. Gwalani, K. Liu, E.J. Faierson, R.S. Mishra, *Addit. Manuf.* 26 (2019) 53–64, doi:10.1016/j.addma.2018.12.015.
- [38] J. Huang, Y. Ren, Y. Jiang, B. Zhang, K. Yang, *Front. Mater. Sci. China* 1 (4) (2007) 405–409, doi:10.1007/s11706-007-0074-1.
- [39] C. Hampp, et al., *Adv. Eng. Mater.* 14 (3) (2012) 28–37, doi:10.1002/adem.201180066.
- [40] Y. Li, et al., *Acta Biomater.* 8 (8) (2012) 3177–3188, doi:10.1016/j.actbio.2012.04.028.
- [41] N.D. Nam, W.C. Kim, J.G. Kim, K.S. Shin, and H.C. Jung, “Corrosion resistance of Mg – 5Al – x Sr alloys,” vol. 509, pp. 4839–4847, 2011, doi: 10.1016/j.jallcom.2011.01.187.
- [42] M. Bornapour, N. Muja, D. Shum-tim, M. Cerruti, M. Pekguleryuz, *Acta Biomater.* 9 (2) (2013) 5319–5330, doi:10.1016/j.actbio.2012.07.045.
- [43] J.M. Seitz, R. Eifler, J. Stahl, M. Kietzmann, F.W. Bach, *Acta Biomater.* 8 (10) (2012) 3852–3864, doi:10.1016/j.actbio.2012.05.024.
- [44] Z. Li, X. Gu, S. Lou, Y. Zheng, *Biomaterials* 29 (10) (2008) 1329–1344, doi:10.1016/j.biomaterials.2007.12.021.
- [45] H.R.B. Rad, M.H. Idris, M.R.A. Kadir, S. Farahany, *Mater. Des.* 33 (1) (2012) 88–97, doi:10.1016/j.matdes.2011.06.057.
- [46] H. Ibrahim, S.N. Esfahani, B. Poorganji, D. Dean, M. Elahinia, *Mater. Sci. Eng. C* 70 (2016) 870–888, doi:10.1016/j.msec.2016.09.069.
- [47] J.Y. Lock, et al., *J. Biomed. Mater. Res. - Part A* 102 (3) (2014) 781–792, doi:10.1002/jbm.a.34741.
- [48] C.M. Campos, et al., *Int. J. Mol. Sci.* 14 (12) (2013) 24492–24500, doi:10.3390/ijms141224492.
- [49] S. Wang, X. Zhang, J. Li, C. Liu, S. Guan, *Bioact. Mater.* 5 (1) (2020) 1–8, doi:10.1016/j.bioactmat.2020.01.002.
- [50] D. Zhao, et al., *Biomaterials* 81 (2016) 84–92, doi:10.1016/j.biomaterials.2015.11.038.
- [51] J. Wu, B. Lee, P. Saha, P.N. Kumta, *J. Biomater. Appl.* 33 (8) (2019) 1080–1093, doi:10.1177/0885328218824775.
- [52] K.F. Farraro, K.E. Kim, S.L.-Y. Woo, B. Jonquil, R. Flowers, Matthew McCullough, *J. Biomech.* 100 (2) (2012) 130–134, doi:10.1016/j.pestbp.2011.02.012. Investigations.
- [53] D. Tang, R.S. Tare, L. Yang, D.F. Williams, K. Ou, R.O.C. Oreffo, *Biomaterials* 83 (2016) 363–382, doi:10.1016/j.biomaterials.2016.01.024.
- [54] J.L. Drury, D.J. Mooney, *Biomaterials* 24 (2003) 4337–4351, doi:10.1016/S0142-9612(03)00340-5.
- [55] S.J. Hollister, *Nat. Mater.* 4 (7) (2005) 518–524.
- [56] D.W. Hutmacher, *J. Biomater. Sci. Polym. Edn.* 12 (1) (2001) 107–124.
- [57] F. Veronesi, et al., *Soc. Biomater.* 103 (9) (2015) 2932–2941, doi:10.1002/jbm.a.35433.
- [58] A. Do, B. Khorsand, S.M. Geary, A.K. Salem, *Adv. Healthc. Mater.* 4 (2015) 1742–1762, doi:10.1002/adhm.201500168.
- [59] B.T.L. Nguyen, M.P. Staiger, G.J. Dias, T.B.F. Woodfield, *Adv. Eng. Mater.* 13 (9) (2011) 872–881, doi:10.1002/adem.201100029.
- [60] S.L. Sing, J. An, W.Y. Yeong, F.E. Wiria, *J. Orthop. Res.* 34 (3) (2016) 369–385, doi:10.1002/jor.23075.
- [61] Z. Wang, W. Wu, G. Qian, L. Sun, X. Li, J.A.F.O. Correia, *Eng. Fract. Mech.* 214 (2019) 149–163, doi:10.1016/j.engfracmech.2019.03.040.
- [62] T. Debroy, et al., *Prog. Mater. Sci. J.* 92 (2018) 112–224.
- [63] K. Wei, M. Gao, Z. Wang, X. Zeng, *Mater. Sci. Eng. A* 611 (2014) 212–222, doi:10.1016/j.msea.2014.05.092.
- [64] M. Salehi, et al., *Powder Technol* 333 (2018) 252–261, doi:10.1016/j.powtec.2018.04.026.

- [65] P. Wang, et al., *Mater. Sci. Eng. A* 711 (2018) 562–570, doi:10.1016/j.msea.2017.11.063.
- [66] H.X. Zhu, A.H. Windle, *Acta Mater.* 50 (2002) 1041–1052.
- [67] C.C. Ng, M.M. Savalani, H.C. Man, I. Gibson, *Virtual Phys. Prototyp.* 5 (1) (2010) 13–19, doi:10.1080/17452751003718629.
- [68] Y. Yang, et al., *Virtual Phys. Prototyp.* 11 (3) (2016) 173–181, doi:10.1080/17452759.2016.1210522.
- [69] B. Song, et al., *Front. Mech. Eng.* 10 (2) (2015) 111–125, doi:10.1007/s11465-015-0341-2.
- [70] R. Xu, et al., *Mater. Lett.* 237 (2019) 253–257, doi:10.1016/j.matlet.2018.11.071.
- [71] J. Chen, et al., *Metals (Basel)* 6 (259) (2016) 1–10, doi:10.3390/met6110259.
- [72] C. Liu, M. Zhang, C. Chen, *Mater. Sci. Eng. A* 703 (2017) 359–371.
- [73] Y. Qin, et al., *Mater. Des.* 181 (107937) (2019) 1–10, doi:10.1016/j.matdes.2019.107937.
- [74] N.A. Zumdick, L. Jauer, L.C. Kersting, T.N. Kutz, J.H. Schleifenbaum, D. Zander, *Mater. Character.* 147 (2019) 384–397, doi:10.1016/j.matchar.2018.11.011.
- [75] K. Wei, et al., *Mater. Sci. Eng. A* 756 (2019) 226–236.
- [76] C. He, et al., *Metals (Basel)* 7 (105) (2017) 1–12, doi:10.3390/met7030105.
- [77] L. Liu, et al., *Materials (Basel)* 10 (477) (2017) 1–11, doi:10.3390/ma10050477.
- [78] B. Zhang, H. Liao, C. Coddet, *Mater. Des.* 34 (2012) 753–758, doi:10.1016/j.matdes.2011.06.061.
- [79] B.R. Sunil, T.S.S. Kumar, U. Chakkingal, V. Nandakumar, M. Doble, *Mater. Sci. Eng. C* 39 (2014) 315–324.
- [80] R. del Campo, B. Savoini, A. Muñoz, M.A. Monge, G. Garcés, *J. Mech. Behav. Biomed. Mater.* 39 (2014) 238–246, doi:10.1016/j.jmbbm.2014.07.014.
- [81] C. Shuai, et al., *Materials (Basel)* 10 (307) (2017) 1–12, doi:10.3390/ma10030307.
- [82] H.T. Ma, et al., *Acta Mater.* 147 (2018) 42–50 Apr., doi:10.1016/j.actamat.2018.01.010.
- [83] W.J. Kim, I.K. Moon, S.H. Han, *Mater. Sci. Eng. A* 538 (2012) 374–385 Mar., doi:10.1016/j.msea.2012.01.063.
- [84] K. Wei, Z. Wang, X. Zeng, *Mater. Lett.* 156 (2015) 187–190.
- [85] M. Zhang, C. Chen, C. Liu, S. Wang, *Metals (Basel)* 8 (635) (2018) 1–19, doi:10.3390/met8080635.
- [86] T. Long, X. Zhang, Q. Huang, L. Liu, Y. Liu, J. Ren, *Virtual Phys. Prototyp.* 0 (0) (2017) 1–11, doi:10.1080/17452759.2017.1411662.
- [87] C. Shuai, Y. Zhou, X. Lin, Y. Yang, C. Gao, J. Mater. Sci. Mater. Med. 28 (13) (2017) 12–19, doi:10.1007/s10856-016-5825-z.
- [88] Y. Li, et al., *Acta Biomater.* 67 (2018) 378–392, doi:10.1016/j.actbio.2017.12.008.
- [89] Y. Li, et al., *Addit. Manuf.* 28 (2019) 299–311.
- [90] L. Zhang, G. Yang, B.N. Johnson, X. Jia, *Acta Biomater.* 84 (2019) 16–33, doi:10.1016/j.actbio.2018.11.039.
- [91] K. Tsai, H. Lin, Y. Chen, C. Lin, T. Hsu, C. Kao, *Materials (Basel)* 65 (10) (2017) 1–14, doi:10.3390/ma10010065.
- [92] C. Shuai, et al., *Mater. Des.* 174 (2019) 107801, doi:10.1016/j.matdes.2019.107801.
- [93] C. Shuai, W. Guo, C. Gao, Y. Yang, P. Wu, P. Feng, *Int. J. Bioprinting* 4 (1) (2018) 1–14.
- [94] H. Sun, et al., *Materials (Basel)* 9 (287) (2016) 1–12, doi:10.3390/ma9040287.
- [95] M. Salehi, S. Maleksaeedi, M. Ling, S. Nai, M. Gupta, *Addit. Manuf.* 29 (100790) (2019) 1–13, doi:10.1016/j.addma.2019.100790.
- [96] D. Karlsson, et al., *Addit. Manuf.* 27 (2019) 72–79, doi:10.1016/j.addma.2019.02.010.
- [97] S. Huang, C. Ye, H. Zhao, Z. Fan, Q. Wei, *Adv. Appl. Ceram.* 6753 (2019) 458–465, doi:10.1080/17436753.2019.1666593.
- [98] A. Yegyan, J. Wang, Y. Bai, S.T. Huxtable, C.B. Williams, *Mater. Des.* 182 (2019) 1–12, doi:10.1016/j.matdes.2019.108001.
- [99] E.M. Wilts, D. Ma, Y. Bai, C.B. Williams, T.E. Long, *ACS Appl. Mater. Interfaces* 11 (2019) 23938–23947, doi:10.1021/acsami.9b08116.
- [100] S. Huang, C. Ye, H. Zhao, Z. Fan, *Mater. Manuf. Process.* 00 (2019) 1–7, doi:10.1080/10426914.2019.1675890.
- [101] X. Lv, F. Ye, L. Cheng, S. Fan, Y. Liu, *Ceram. Int.* 45 (10) (2019) 12609–12624, doi:10.1016/j.ceramint.2019.04.012.
- [102] A. Mostafaei, et al., *Mater. Sci. Eng. C* 102 (2019) 276–288, doi:10.1016/j.msec.2019.04.011.
- [103] I. Polozov, V. Sufiiarov, A. Shamshurin, *Mater. Lett.* 243 (2019) 88–91, doi:10.1016/j.matlet.2019.02.027.
- [104] C.L. Cramer, P. Nandwana, R.A. Lowden, A.M. Elliott, *Addit. Manuf.* 28 (2019) 333–343.
- [105] K. Kimes, K. Myers, A. Klein, M. Ahlfors, E. Stevens, *Microsc. Microanal.* 25 (2019) 2600–2601, doi:10.1017/S1431927619013734.
- [106] T. Brückner, U. Gbureck, *AME Med. J.* (2017) 51–51, Mar., doi:10.21037/amj.2017.04.01.
- [107] M.M. Farag, H. Yun, *Mater. Lett.* 132 (2014) 111–115, doi:10.1016/j.matlet.2014.06.055.
- [108] E. Vorndran, et al., *Adv. Appl. Ceram.* 110 (8) (2013) 476–481, doi:10.1179/1743676111Y.0000000030.
- [109] S. Meininger, S. Mandal, A. Kumar, J. Groll, B. Basu, U. Gbureck, *Acta Biomater.* 31 (2015) 401–411, doi:10.1016/j.actbio.2015.11.050.
- [110] M. Salehi, et al., *Acta Mater.* 165 (2019) 294–306, doi:10.1016/j.actamat.2018.11.061.
- [111] M. Salehi, et al., *Mater. Des.* 169 (107683) (2019) 1–15, doi:10.1016/j.matdes.2019.107683.
- [112] A.H. Yusop, A.A. Bakir, N.A. Shaharom, M.R.A. Kadir, H. Hermawan, *Int. J. Biomater.* 2012 (2012) 1–10, doi:10.1155/2012/641430.
- [113] M.P. Staiger, I. Kolbeinson, N.T. Kirkland, T. Nguyen, G. Dias, T.B.F. Woodfield, *Mater. Lett.* 64 (2010) 2572–2574, doi:10.1016/j.matlet.2010.08.049.
- [114] R.N. Oosterbeek, C.K. Seal, M.P. Staiger, M.M. Hyland, *Soc. Biomater.* 103 (1) (2014) 311–317.
- [115] W. Lin, B.E. Franco, I. Karaman, A. Elwany, J. Ma, *Mater. Sci. Eng. C* 105 (109747) (2019) 1–9, doi:10.1016/j.msec.2019.109747.
- [116] N. Kleger, M. Cihova, K. Masania, A.R. Studart, J.F. Löffler, *Adv. Mater.* 1903783 (2019) 1–10, doi:10.1002/adma.201903783.
- [117] J. Parthasarathy, B. Starly, S. Raman, A. Christensen, *J. Mech. Behav. Biomed. Mater.* 3 (3) (2010) 249–259, doi:10.1016/j.jmbbm.2009.10.006.
- [118] S. Arabnejad, R.B. Johnston, J. Ann, B. Singh, M. Tanzer, D. Pasini, *Acta Biomater.* 30 (2016) 345–356, doi:10.1016/j.actbio.2015.10.048.
- [119] C. Yan, L. Hao, A. Hussein, D. Raymont, *Int. J. Mach. Tools Manuf.* 62 (2012) 32–38, doi:10.1016/j.ijmactools.2012.06.002.
- [120] D.A. Hollander, et al., *Biomaterials* 27 (2006) 955–963, doi:10.1016/j.biomaterials.2005.07.041.
- [121] L. Mullen, R.C. Stamp, P. Fox, E. Jones, C. Ngo, C.J. Sutcliffe, *J. Biomed. Mater. Res. Part B Appl. Biomater.* 92 (1) (2009) 178–188, doi:10.1002/jbm.b.31504.
- [122] X. Song, M. Xie, F. Hofmann, T. Illston, T. Connolley, *Int. J. Mater. Form.* 8 (2015) 245–254, doi:10.1007/s12289-014-1163-1.
- [123] Z. Xiao, Y. Yang, R. Xiao, Y. Bai, C. Song, D. Wang, *Mater. Des.* 143 (2018) 27–37, doi:10.1016/j.matdes.2018.01.023.
- [124] J.R. Croteau, et al., *Acta Mater.* 153 (2018) 35–44, doi:10.1016/j.actamat.2018.04.053.
- [125] C.C. Ng, M. Savalani, H.C. Man, *Rapid Prototyp. J.* 6 (17) (2011) 479–490, doi:10.1108/13552541111184206.
- [126] T. Lee, M. Yamasaki, Y. Kawamura, Y. Lee, C. Soo, *Mater. Lett.* 234 (2019) 245–248, doi:10.1016/j.matlet.2018.09.090.
- [127] T. Lee, M. Yamasaki, Y. Kawamura, J. Go, S.H. Park, *Met. Mater. Int.* 25 (2019) 372–380.
- [128] X. Niu, H. Shen, J. Fu, J. Yan, Y. Wang, *Corros. Sci.* 157 (2019) 284–294, doi:10.1016/j.corsci.2019.05.026.
- [129] N. Sezer, Z. Evis, S.M. Kayhan, A. Tahmasebifar, M. Koç, *J. Magnes. Alloy.* 6 (2018) 23–43, doi:10.1016/j.jma.2018.02.003.
- [130] C. Shuai, Y. Yang, P. Wu, X. Lin, Y. Liu, Y. Zhou, *J. Alloys Compd.* 691 (2017) 961–969, doi:10.1016/j.jallcom.2016.09.019.
- [131] S.Y. He, Y. Sun, M.F. Chen, D.B. Liu, X.Y. Ye, *Trans. Nonferrous Met. Soc. China* 21 (4) (2011) 814–819, doi:10.1016/S1003-6326(11)60786-3.

- [132] Y. Huang, D. Liu, L. Anguilano, C. You, M. Chen, *Mater. Sci. Eng. C* 54 (2015) 120–132, doi:10.1016/j.msec.2015.05.035.
- [133] Y. Yan, et al., *Mater. Sci. Eng. C* 74 (2017) 582–596.
- [134] Y. Deng, et al., *Int. J. Bioprinting* 4 (4) (2018) 1–11.
- [135] C. Shuai, Y. Yang, S. Peng, C. Gao, P. Feng, J. Mater. Sci. Mater. Med. 28 (130) (2017) 129–140, doi:10.1007/s10856-017-5945-0.
- [136] M.-C. Zhao, M. Liu, G. Song, A. Atrens, *Corros. Sci.* 50 (2008) 1939–1953.
- [137] M. Alvarez-lopez, et al., *Acta Biomater.* 6 (5) (2010) 1763–1771, doi:10.1016/j.actbio.2009.04.041.
- [138] C. Shuai, et al., *Virtual Phys. Prototyp.* 13 (2) (2018) 59–69, doi:10.1080/17452759.2017.1408918.
- [139] Y. Yang, X. Guo, C. He, C. Gao, C. Shuai, *ACS Biomater. Sci. Eng.* 4 (2018) 1046–1054, doi:10.1021/acsbomaterials.8b00020.
- [140] L. Yuan, S. Ding, C. Wen, *Bioact. Mater.* 4 (1) (2019) 56–70, doi:10.1016/j.bioactmat.2018.12.003.
- [141] L.J. Gibson, *J. Biomech.* 38 (3) (2005) 377–399, doi:10.1016/j.jbiomech.2004.09.027.
- [142] E. Hall, *Yield Point Phenomena in Metals and Alloys*, Springer, 2012.
- [143] C.C. Ng, M.M. Savalani, M.L. Lau, H.C. Man, *Appl. Surf. Sci.* 257 (2011) 7447–7454, doi:10.1016/j.apsusc.2011.03.004.
- [144] Y. Zhang, Y. Li, H. Liu, J. Bai, N. Bao, Y. Zhang, *Orthop. Surg.* 10 (2) (2018) 160–168, doi:10.1111/os.12378.
- [145] S. Liu, W. Yang, X. Shi, B. Li, S. Duan, *J. Alloys Compd.* 808 (151160) (2019) 1–16, doi:10.1016/j.jallcom.2019.06.261.
- [146] S.M. Ahmadi, et al., *J. Mech. Behav. Biomed. Mater.* 34 (2014) 106–115, doi:10.1016/j.jmbbm.2014.02.003.
- [147] M. Fousová, D. Vojt, E. Jablonská, J. Fojt, *J. Mech. Behav. Biomed. Mater.* 69 (2017) 368–376, doi:10.1016/j.jmbbm.2017.01.043.
- [148] X. Dong-ming, Y. Yong-qiang, S.U. Xu-bin, W. Di, L.U.O. Zi-yi, *Trans. Nonferrous Met. Soc. China* 22 (2012) 2554–2561, doi:10.1016/S1003-6326(11)61500-8.
- [149] S. Yin, W. Zhang, Z. Zhang, X. Jiang, *Adv. Healthc. Mater.* 1801433 (2019) 1–19.
- [150] J. Rouwkema, N.C. Rivron, C.A. Van Blitterswijk, *Trends Biotechnol.* 26 (8) (2008) 434–441, doi:10.1016/j.tibtech.2008.04.009.
- [151] J. Trinidad, et al., *Adv. Eng. Mater.* 16 (2) (2014) 241–247, doi:10.1002/adem.201300236.
- [152] F. Liu, B. Huang, S. Hinduja, J. Paulo, S. Bartolo, *Bioceram. Biocompos.: From Res. Clin. Pract.* (2019) 17–37.
- [153] C. Wu, J. Chang, W. Zhai, *J. Mater. Sci. Mater. Med.* 18 (2007) 857–864, doi:10.1007/s10856-006-0083-0.
- [154] S. Thelen, F. Barthelat, L.C. Brinson, *J. Biomed. Mater. Res. Part A* 69 (4) (2004) 601–610, doi:10.1002/jbm.a.20100.
- [155] T.M. Freyman, I.V. Yannas, L.J. Gibson, *Prog. Mater. Sci.* 46 (2001) 273–282.
- [156] N. Jasmawati, J.R.P. Djuansjah, M.R.A. Kadir, I. Sukmana, *Adv. Mater. Res.* 1125 (2015) 437–440 doi:10.4028/www.scientific.net/AMR.1125.437.
- [157] A.A. Zadpoor, *Biomater. Sci.* 3 (2015) 231–245, doi:10.1039/c4bm00291a.
- [158] C.M. Bidan, F.M. Wang, J.W.C. Dunlop, C.M. Bidan, F.M. Wang, J.W.C. D.A., *Comput. Methods Biomech. Biomed. Engin.* 16 (10) (2013) 1056–1070 Taylor & Francis, doi:10.1080/10255842.2013.774384.
- [159] E. Gamsjäger, C.M. Bidan, F.D. Fischer, P. Fratzl, J.W.C. Dunlop, *Acta Biomater.* 9 (2013) 5531–5543, doi:10.1016/j.actbio.2012.10.020.
- [160] U. Ripamonti, L.C. Roden, L.F. Renton, *Biomaterials* 33 (15) (2012) 3813–3823, doi:10.1016/j.biomaterials.2012.01.050.
- [161] J.K. Nychala, N.B. Oupoulos, C.J.C. Att, O.L.K. Atsamenis, C.P.P. Lease, B.G.S. Engers, *Ann. Biomed. Eng.* 41 (5) (2013) 917–930, doi:10.1007/s10439-013-0748-z.
- [162] M. Bidan, et al., *PLoS ONE* 7 (5) (2012) 1–11, doi:10.1371/journal.pone.0036336.
- [163] C.M. Bidan, K.P. Kommareddy, M. Rumpler, P. Kollmannsberger, P. Fratzl, J.W.C. Dunlop, *Adv. Healthc. Mater.* 2 (2013) 186–194, doi:10.1002/adhm.201200159.
- [164] V.E. Beal, R.A. Paggi, G.V. Salmoria, A. Lago, *J. Appl. Polym. Sci.* 113 (2009) 2910–2919, doi:10.1002/app.
- [165] K.C.R. Kolan, M.C. Leu, G.E. Hilmas, M. Velez, *J. Mech. Behav. Biomed. Mater.* 13 (2012) 14–24, doi:10.1016/j.jmbbm.2012.04.001.
- [166] D. Gu, Y. Hagedorn, W. Meiners, G. Meng, *Acta Mater.* 60 (2012) 3849–3860, doi:10.1016/j.actamat.2012.04.006.
- [167] E.O. Olakanmi, R.F. Cochrane, K.W. Dalgarno, *Prog. Mater. Sci.* 74 (2015) 401–477, doi:10.1016/j.pmatsci.2015.03.002.
- [168] L. Thijs, F. Verhaeghe, T. Craeghs, J. Van Humbeeck, J. Kruth, *Acta Mater.* 58 (9) (2010) 3303–3312, doi:10.1016/j.actamat.2010.02.004.
- [169] N.T. Aboulkhair, N.M. Everitt, I. Ashcroft, C. Tuck, *Addit. Manuf.* 1–4 (2014) 77–86, doi:10.1016/j.addma.2014.08.001.
- [170] S. Farid, Seyed Shirazi, et al., *Sci. Technol. Adv. Mater.* 16 (2015) 1–20, doi:10.1088/1468-6996/16/3/033502.
- [171] W.M. Tucho, V.H. Lysne, H. Austbø, A. Sjolyst-kverneland, *J. Alloys Compd.* 740 (2018) 910–925, doi:10.1016/j.jallcom.2018.01.098.
- [172] G. Wang, et al., *Mater. Sci. Eng. C* 32 (8) (2012) 2190–2198, doi:10.1016/j.msec.2012.05.050.
- [173] S.L. Sing, L.P. Lam, D.Q. Zhang, Z.H. Liu, C.K. Chua, *Mater. Charact.* 107 (2015) 220–227, doi:10.1016/j.matchar.2015.07.007.
- [174] A. Pawlak, M. Rosienkiewicz, E. Chlebus, *Arch. Civ. Mech. Eng.* 17 (2017) 9–18, doi:10.1016/j.acme.2016.07.007.
- [175] X. Ji, E. Mirkoohi, J. Ning, S.Y. Liang, *Opt. Lasers Eng.* 124 (105805) (2020) 1–9, doi:10.1016/j.optlaseng.2019.105805.
- [176] J. Li, X. Cheng, Z. Li, X. Zong, S. Zhang, H. Wang, *Mater. Sci. Eng. A* 735 (2018) 408–417, doi:10.1016/j.msea.2018.08.074.
- [177] Y. Yang, G. Wang, H. Liang, C. Gao, S. Peng, L. Shen, *Int. J. Bioprinting* 5 (1) (2019) 1–25.
- [178] A. Kopp, et al., *Acta Biomater.* (2019) In Press.
- [179] S. Kimura, T. Nakamoto, T. Ozaki, K. Sugita, M. Mizuno, *Mater. Sci. Eng. A* 754 (2019) 786–798, doi:10.1016/j.msea.2019.02.015.
- [180] X. Cao, M. Jahazi, J.P. Immarigeon, W. Wallace, *J. Mater. Process. Technol.* 171 (2006) 188–204, doi:10.1016/j.jmatprotec.2005.06.068.
- [181] M. Gieseke, C. Noelke, S. Kaieler, V. Wesling, H. Haferkamp, *B. Implants, Magnes. Technol.* 1 (2013) 65–68.
- [182] X. Tan and Y.J. Tan, *3D Printing of Metallic Cellular Scaffolds for Bone Implants*. 2019.
- [183] H. Takagi, et al., *Addit. Manuf.* 24 (2018) 498–507 no. July, doi:10.1016/j.addma.2018.10.026.
- [184] D.D. Gu, et al., *Int. Mater. Rev.* 57 (2013) 133–164, doi:10.1179/1743280411Y.0000000014.